# Thermophysical characteristics and enhancement analysis of carbon–additives phase change mono and hybrid materials for thermal management of electronic devices.

Adeel Arshad[a,*], Mark Jabbal[a], Lei Shi[a,c], Yuying Yan[a,b,*]

[a]*Fluids & Thermal Engineering (FLUTE) Research Group, Faculty of Engineering, University of Nottingham, Nottingham, NG7 2RD, UK*
[b]*Research Centre for Fluids and Thermal Engineering, University of Nottingham Ningbo China, Ningbo 315100, China*
[c]*School of Energy Science and Engineering, Harbin Institute of Technology, Harbin 150001, China*

---

## Abstract

A novel zero–noise and clean thermal management technology (TMT), based on phase–change thermal energy storage (TES) technology, has turned out the new vision for researchers and industrialist involved in electronics industry. Therefore, this paper highlights a new direction by developing the nano–enhanced phase change materials (NePCMs) by combing the carbon–additives with phase change material. Four different types of carbon–additives of multi–wall carbon nanotube (MWCNT), graphene oxide (GO), reduced graphene oxide (rGO) and graphene nanoplatelet (GNP) were dispersed in RT–35HC, used as a PCM, with the combinations of mono (MWCNT, GO, rGO and GNP) and hybrid (GO+MWCNT, rGO+MWCNT and GNP+MWCNT) nanoparticles. A constant mass percentage of 1.0 wt.% was selected for both mono and hybrid combinations of nanoparticles to explore the best type and dispersion scheme for productive and effective thermal management applications. All the synthesised NePCMs were characterized using various characterization methods to study microstructural features, surface chemistry, lattice dimensions, stability, thermal and phase–change TES characteristics. The key findings reveal the best chemical and thermal stability, uniform dispersion of carbon–based nanoparticles in RT–35HC without modifying the molecular structure. The highest thermal conductivity enhancements of 182.7%, 183.8% and 185.3%, and optimum value of enthalpy of fusions of 237.42, 235.35 and 230.82 J/g were achieved for hybrid $\text{NePCM}_{GO+MWCNT}$, $\text{NePCM}_{rGO+MWCNT}$, and $\text{NePCM}_{GNP+MWCNT}$, respectively. in comparison of mono NePCMs. The phenomenon of

---

[*] Correspondence authors
*Email addresses:* `adeel.arshad@nottingham.ac.uk`, `adeel_kirmani@hotmail.com` (Adeel Arshad), `yuying.yan@nottingham.ac.uk` (Yuying Yan)

*Preprint submitted to Journal of Energy Storage* *December 7, 2020*

thermal conductivity and specific heat capacity were explained systematically. Conclusively, the minimum subcooling, specific heat capacity enhancement and smaller phase–transition temperature reveal that GNP+MWCNT dispersed hybrid NePCM can be potentially used for thermal management applications.

*Keywords:* Thermal management technology, Nano–enhanced phase change materials, MWCNT, GO, rGO, GNP, Phase change material

## 1. Introduction

In current century, the revolutionary advancement in microelectronics including the miniaturization and parallel multi–functions performance demands a novel thermal management cooing solution. This progressing trend has led towards the development of micro level electronic components with higher power level. Thence, a serious challenge has been rising of overheating within the internal circuits of electronic devices which is deteriorating the operating features and lifetime performance. To overcome this challenge, there exists an emerging need of a novel thermal cooling technology which can sustain the cooling performance and operating life of electronic devices. A *quiet* and *clean* cooling technology with *zero* power consumption has a remarkable introduction in advanced smart cooling technologies, based on the latent–heat thermal energy storage (LHTES) system [1]. Such a cleaner sustainable energy technology LHTES system is integrated with materials that have an intrinsic potential of absorbing and releasing the thermal energy. These materials are called phase change materials (PCMs) which can store the large amount of heat because of high energy storage density during charging and discharging cycles. The melting and solidification enthalpies of the PCMs are effectively utilized when integrated with a cooling system and thermal loads can be controlled through operating parameters [2]. In spite of that, PCMs exhibit some issues mainly lower thermal conductivity, super–cooling, less thermal stability, etc. which reduce the heat transfer performance while cooling. Recently, the different design and material aspects of PCM based cooling systems have been explored such as the leakage phenomenon [3], structure design [4], enhancing the mechanical properties [5] and evaluating the long-term durability [6].

The energy technologists and researchers have been contributing the great efforts to improve the thermophysical properties by adopting various performance enhancement techniques such as by dispersing the nanomaterials, encapsulation, shape–stabilization and embedding metal–foams [7], metallic fins [8] or heat pipes [9, 10]. These days addition of highly thermal conductive matrix and chemically treated surfaces of nanomaterials have taken over the key attention for researchers and scientist. Surface modification and grafting functional groups are the main methods along with the addition of three–dimensional (3D), two–dimensional (2D), one–dimensional (1D) and zero–dimensional (0D) structural additives [11]. Nanomaterials additives including nanoparticles, nanosheets, nanotubes, nanofibers, nanorods, nanowires and quantum dots exhibit a specific structural configuration [11].The addition of nanomaterials have been evaluated to improve the thermal conductivity and specific heat and to reduce the interfacial thermal resistance. The addition of nanomaterials in PCMs form a thermal conduction path, reduce the phonon scattering and enhance the heat transfer rate. The carbon–based nanomaterials family, which possess all the dimensionality and morphology, have proven the remarkable thermophysical properties for the applications of LHTES and thermal management systems when added into the PCMs [12, 13]. For instance, Choi et al. [14] synthesized the NePCMs using three different carbon additives such as MWCNTs, graphite, and graphene to determine the thermal conductivity for TES applications. The authors used the hot–wire method and found that graphene showed the highest thermal conductivity enhancement of 21.5% at 0.1 vol.% loading. Moreover, they obtained the enhancement in heat transfer up to 3.35 times higher with 5.0 vol.% of graphite. Li et al. [15] used the grafted CNT by grafting polyhydric alcohol and mixed into the paraffin as a PCM to prepare the NePCMs. Results showed the 38% graft ratio of stearyl alcohol grafted CNT and found the highest thermal conductivities of 0.7903 W/m.K at 4 wt.%. Li et al. [16] selected the MWCNT, graphene and graphite as a carbon additives and stearic acid as a PCM to prepare the phase change NePCMs for TES applications. Results revealed that by adding the carbon additives the heat conduction mode improved whereas heat convection mode was weakened. The best charging and discharging rates were obtained around 37% and 320%, respectively, with 5.0% of graphite added NePCM. Moreover, a 12 times enhancement was obtained in thermal conductivity with 5.0% of graphite added NePCM. Fan et al. [17] tested the CNT and GNP based composite PCM in heat sink for TES application at various concentrations. The authors determined the various thermophysical properties and found the 5.3% and 7.3% reduction in latent–heat fusion for CNT and GNP based composite PCM, respectively, at 3 wt.%. The thermal conductivity was enhanced of 31.1% and 170% for CNT and GNP based composite PCM, respectively, at 3 wt.%. Bahiraei et al. [18] conducted the experimental and numerical study based on composite PCM by using CNF, GNP and graphite nanoparticles. Maximum thermal conductivity enhancements were obtained using graphite nanoparticles at 7.5 wt.% and 10 wt.% about 620% and 1100%, respectively, in solid–phase. Zou et al. [19] synthesised the carbon additives (MWCNT and graphene) and paraffin based composite PCM for Li–ion battery cooling application. Authors found the higher thermal conductivity enhancement with 3/7 mass ratio of MWCNT/graphene of 31.8%, 55.4% and 124% compared with GNP, MWCNT and pure PCM, respectively. Recently, Li et al. [20] prepared the composite PCM using sodium sulfate decahydrate ($Na_2SO_4.10H_2O$) and expanded graphite (EG) for

TES application. The results revealed that by dispersing 7 wt.% of EG, the latent–heat of melting and cooling were obtained of 114.0 and 105.5 J/g, respectively. In addition, the thermal conductivity was obtained of 1.96 W/m.k.

The literature reveals that most of the studies focused on TES applications of composite PCMs. In this study, four different carbon additives (MWCNT, GO, rGO and GNP) were dispersed in the RT–35HC in two different schemes: mono and hybrid. A constant loading content of 1.0 wt.% was considered for both mono (MWCNT, GO, rGO and GNP) and hybrid (GO+MWCNT, rGO+MWCNT and GNP+MWCNT) NePCMs. The ratio between hybrid nanoparticles of GO+MWCNT, rGO+MWCNT and GNP+MWCNT was kept constant of 3:1. A detailed experimentation was carried out to investigate the surface structure, chemical and physical interaction, thermal conductivity, specific heat capacity, phase–change enthalpies of solid–liquid and liquid–solid stages, degree of supercooling, chemical and thermal stability of NePCMs as a function of temperature. In addition, the thermal conductivity enhancement mechanism and modes of specific heat capacity enhancement were explained schematically. Finally, this work contributes significantly to the area of thermal management of electronic systems.

## 2. Research Methodology

### 2.1. Materials selection

A commercially available an organic PCM, namely RT-35HC was chosen having phase transition temperature of 34-36 °C which was purchased from Rubitherm GmbH, Germany. Table 1 is summarized the thermophysical properties of RT–35HC. Four different carbon–based nanomaterials such as graphene nanoplatelet (GNP), graphene oxide (GO), reduced graphene oxide (rGO) and multiwall carbon nanotube (MWCNT) were selected as a thermal conductive materials (TCMs). The GNP (thickness <3-5 nm, lateral diameter <10$\mu$m and carbon purity 98 ± 1.0 wt.%), GO (flake thickness: ≤2 nm, lateral diameter: <4$\mu$m and carbon purity: 60 ± 5.0 wt.%) and rGO (flake thickness: <100 nm, lateral diameter: <20$\mu$m and carbon purity: 85 ± 7.5 wt.%) were obtained from 2–Dtech Ltd/Versarien PLC, UK [21]. The MWCNT (outer diameter $5 - 15$nm and length of $10 - 30\mu$m, and purity $> 95$ wt.%) was procured from Carbon Nanotubes Plus, USA [22]. The sodium dodecylbenzene sulfonate (SDBS) was purchased from Sigma-Aldrich, UK. All materials are utilized without carrying out any further chemical processing.

Table 1: *Thermophysical properties of PCM (RT–35HC) [23].*

| Physical properties | RT–35HC |
|---|---|
| Melting temperature (°C) | 34–36 |
| Heat storage capacity (kJ/kg) | 240 |
| Thermal conductivity (W/m.K) | 0.2 |
| Specific heat capacity (J/kg.K) | 2000 |
| Density (kg/m$^3$) | 880 (solid)<br>770 (liquid) |

### *2.2. Preparation of NePCMs composites*

In present study, a two–step method was adopted to synthesize the composite of NePCMs which has been reported extensively [24]. Figure 1 illustrates complete schematic representation of all mono and hybrid samples of NePCMs. RT–35HC was used as a base PCM and GNP, GO, rGO and MWCNT were added as additives to enhance the thermophysical properties of RT–35HC. The mass loading of the additives was kept constant of 1.0 wt.% for both mono and hybrid NePCMs. Additionally, sodium dodecylbenzene sulfonate (SDBS) was added with the ratio 4 : 1 for each loading of the GNP, GO, rGO and MWCNT nanoparticles. While synthesising the hybrid NePCMs, the MWCNT was mixed simultaneously with GNP, GO and rGO keeping the total mass concentration of 1.0 wt.%. The ratio of mass concentration of hybrid NePCMs (GNP/MWCNT, GO/MWCNT and rGO/MWCNT) was kept 75%/25% of 1.0 wt.%.

In first step of NePCMs preparation, the PCM, RT–35HC, was melted until it did not shift into the liquid-phase by using a hot–water bath maintaining at 70 °C temperature constantly. A constant ratio of SDBS was mixed into the liquid RT–35HC as surfactant to improve dispersion of GNP, GO, rGO and MWCNT nanoparticles in RT–35HC more uniformly. As a kind of anionic surfactant, SDBS has good surface activity and strong hydrophilicity thus it effectively reduces the tension of PCM surface during synthesizing the NePCMs. Then the mixture of RT–35HC/SDBS was stirred for 30 min using a magnetic stirrer at rate of 450 rpm and temperature of 70 °C. After that, GNP, GO, rGO, MWCNT, GNP/MWCNT, GO/MWCNT and rGO/MWCNT were added separately to prepare the desired mono and hybrid NePCMs. To achieve the homogeneous and stable dispersion of additives, the stirring of mixture was further continued for 3 hrs to improve the thermophysical properties and uniform melting/cooling of NePCMs. The sample were labelled as NePCM$_{MWCNT}$, NePCM$_{GO}$, NePCM$_{rGO}$, NePCM$_{GNP}$, NePCM$_{GNP+MWCNT}$,

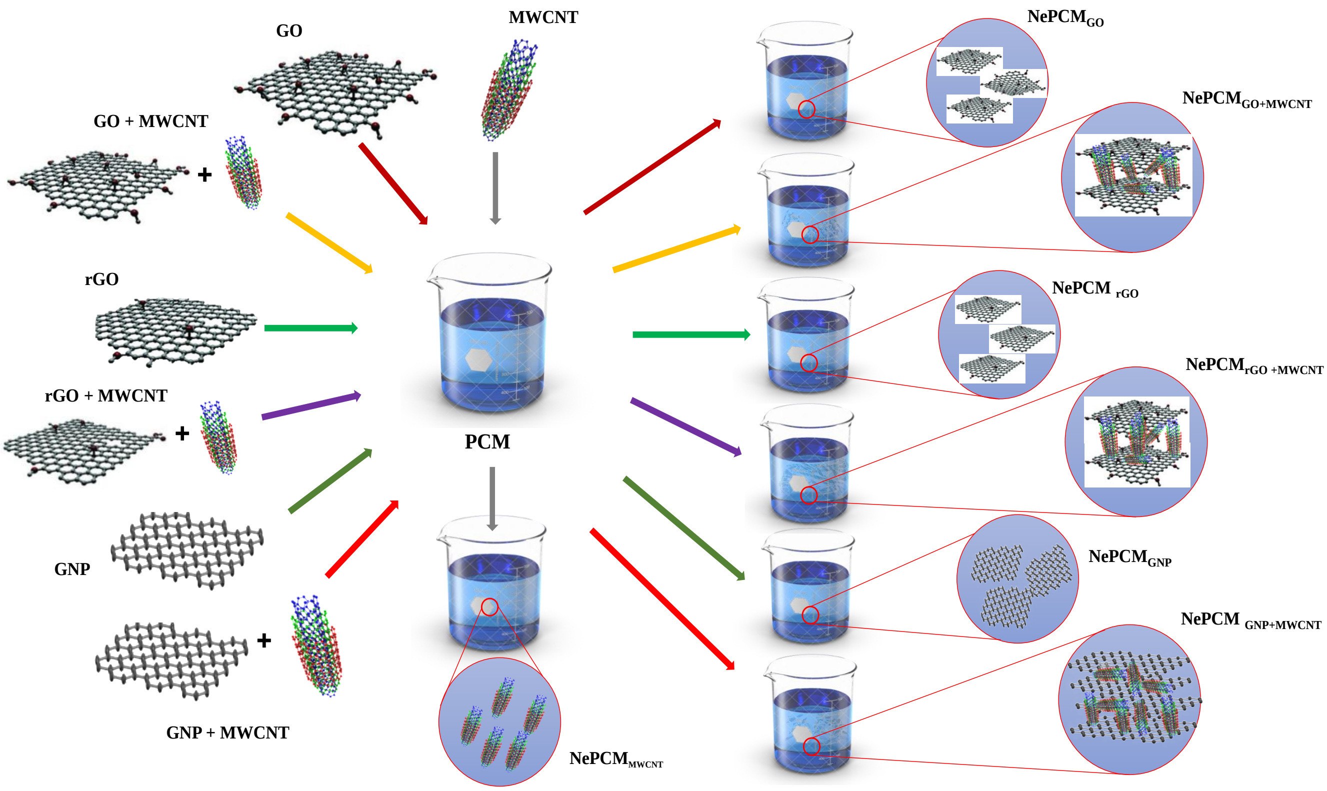

Figure 1: *Schematic diagram of samples preparation of carbon–additives mono and hybrid NePCMs.*

NePCM$_{GO+MWCNT}$ and NePCM$_{rGO+MWCNT}$, based on the mono and hybrid carbon–additives scheme.

In second step of NePCMs preparation, all the samples were sonicated using probe at 40 kHz frequency for 60 min to enhance the homogeneity and dispersion of carbon–additives and to minimize the sedimentation and aggregation. A uniform dispersion of all mono and hybrid carbon-additives used in current can be seen from photographs of prepared samples both in liquid and solid states shown in Figures 2 and 3, respectively. Later on, all the samples of NePCMs were cooled at the ambient temperature.

### *2.3. NePCMs characterizations*

To study the physical, chemical and thermal properties of synthesised NePCMs, different characterization techniques were carried out including ESEM, FTIR, XRD, DSC, TGA and thermal conductivity analyser (TCA).

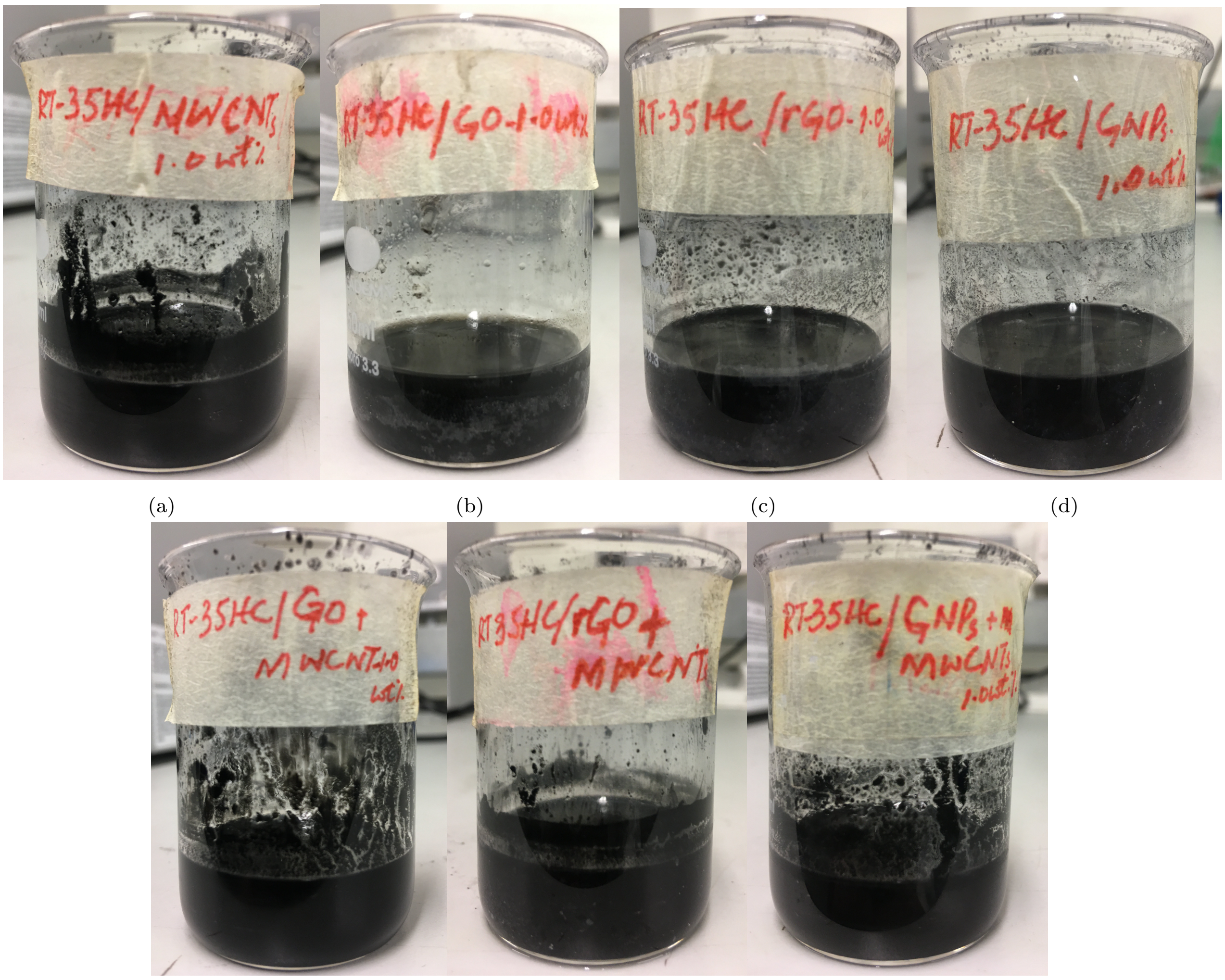

(a) (b) (c) (d)

(e) (f) (g)

Figure 2: *NePCMs after 5 mins: (a) $NePCM_{MWCNT}$, (b) $NePCM_{GO}$, (c) $NePCM_{rGO}$, (d) $NePCM_{GNP}$, (e) $NePCM_{GO+MWCNT}$, (f) $NePCM_{rGO+MWCNT}$, (g) $NePCM_{GNP+MWCNT}$.*

### *2.3.1. Physical and chemical analysis*

To visualize the microstructural features, surface topography and dispersion of carbon–additives in NePCMs, an environmental scanning electron microscopy (ESEM, FEI Quanta–650) was used. To study the chemical composition and record the absorption spectra of powdered GNP, GO, rGO, MWCNT, RT–35HC and synthesized NePCMs at room temperature, fourier transform infrared spectroscope (FTIR, Bruker Tensor–27) was employed. The tests were conducted between wavelength range of $500 - 4000$ cm$^{-1}$ with spectral resolution and accuracy of 4 cm$^{-1}$ and 0.01 cm$^{-1}$, respectively. The study lattice planes and crystallographic structure of powdered GNP, GO, rGO, MWCNT, RT–35HC and synthesized NePCMs, the X–ray diffraction (XRD) patterns were obtained by using Bruker D8–Advance with Da Vinci (Bruker (UK) Ltd) with a monochromatic Cu–K$\alpha$ radiation ($\lambda = 1.5406\mathring{A}$) from angle $2\theta$ range between 5° to 60°.

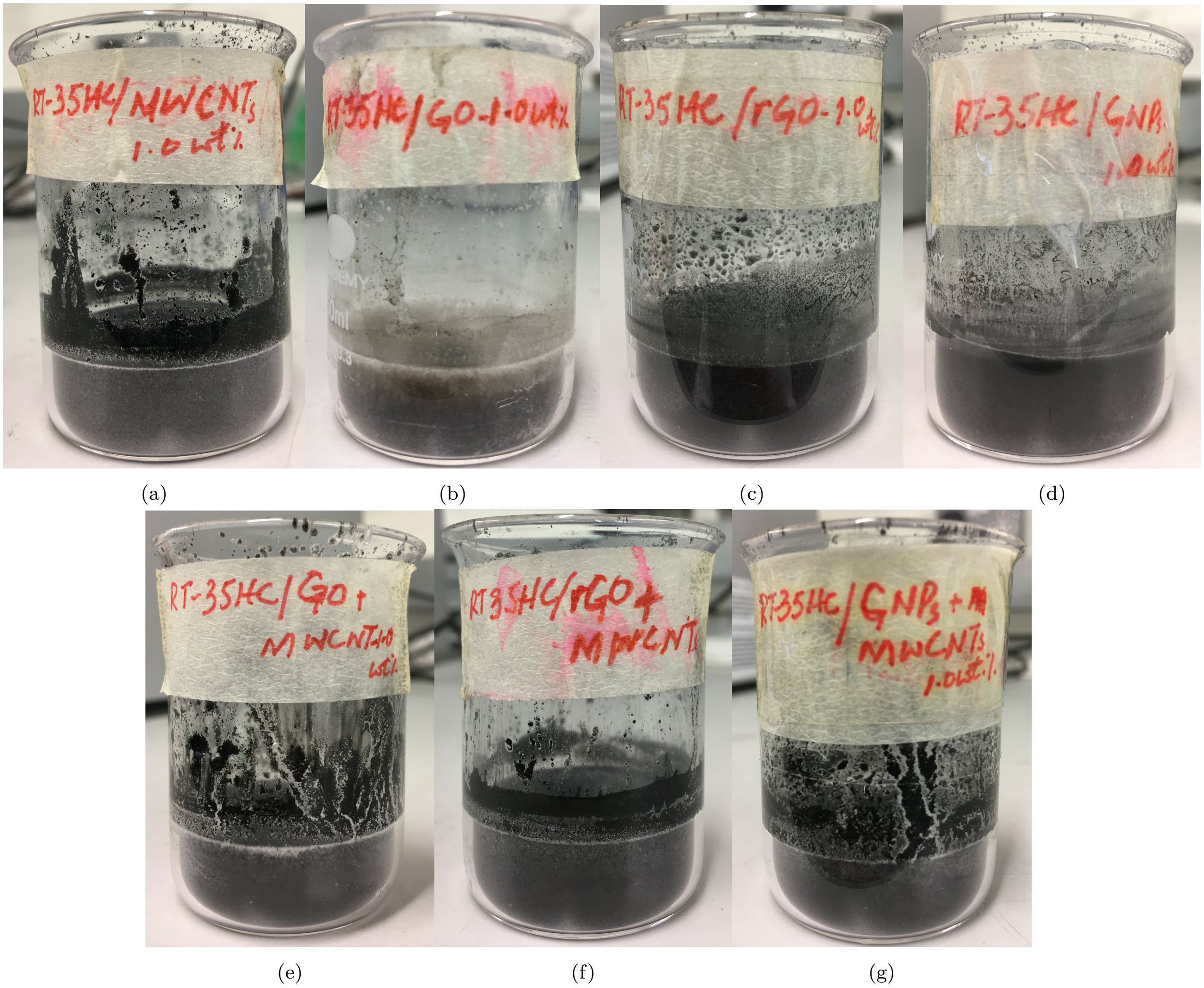

Figure 3: *NePCMs after 50 mins: (a) $NePCM_{MWCNT}$, (b) $NePCM_{GO}$, (c) $NePCM_{rGO}$, (d) $NePCM_{GNP}$, (e) $NePCM_{GO+MWCNT}$, (f) $NePCM_{rGO+MWCNT}$, (g) $NePCM_{GNP+MWCNT}$.*

### *2.3.2. Thermal analysis*

The thermal conductivity was measured of all samples using thermal conductivity analyser (TCA) TCi$^{TM}$ by C–Therm Technologies Ltd. Canada, as a function of temperature (20-55 °) by adopting the modified transient plane source (MTPS) method (ASTM–D7984) [25]. The TCA instrument has the capability to measure thermal conductivity range from 0-500 W/m.K with 5% accuracy and 1% precision. Five readings are recorded for each sample at a specific temperature and average value is reported. A maximum relative error and uncertainty were obtained of ±2.0% and ±1.0%, respectively. The thermal stability of all samples were analysed using thermogravimetric analysis (TGA) and derivative thermogravimetry analysis (DTGA), obtained from SDT–Q600 TA instrument Inc., UK [26] having the precision of 0.1 $\mu$g. A sample mass of about 5-7 mg was filled in a pan, made of aluminium, and three different tests were heated at a rate of 10 °Cmin$^{-1}$ from temperature

20 °C to 400 °C under pure $N_2$ environment of purging flow rate of 100 mLmin$^{-1}$. The phase–transition temperatures and latent–heat enthalpies of all samples were determined by employing differential scanning calorimeter (DSC-2500, TA instrument Inc., UK) while endothermic and exothermic processes [27]. Three tests were performed for each sample from temperature range 10 °C to 50 °C at constant temperature rate of 1 °Cmin$^{-1}$ under $N_2$ flow conditions with accuracy and precision of ±0.04% and ±0.005°C, respectively. The specific heat capacity of all samples was measured at constant heating rate of 3 °Cmin$^{-1}$ from temperature 10 °C to 50 °C by following Sapphire-method. A sample mass of about 3-5 mg was sealed inside a Tzero Hermetic pan, made of aluminium, with the lid to avoid any leakage.

## 3. Results and discussions

### *3.1. Surface morphology analysis*

The surface morphology and microstructural features of GNP, GO, rGO and MWCNT based mono and hybrid NePCMs are shown in Figure 4. The surficial microstructure of pure RT–35HC, NePCM$_{MWCNT}$, NePCM$_{GO}$, NePCM$_{GO+MWCNT}$, NePCM$_{rGO}$, NePCM$_{rGO+MWCNT}$, NePCM$_{GNP}$ and NePCM$_{GNP+MWCNT}$ are presented in Figure 4a, 4b, 4c, 4d, 4e, 4f, 4g and 4h, respectively. The uniform dispersion of GNP, GO, rGO and MWCNT can be visualized from Figure 4 in all mono and hybrid NePCMs because of the repulsive bonding of the SDBS, acting as a dispersing agent. Although the mass faction of GNP, GO, rGO and MWCNT is constant and very less, even though a uniform dispersion and enough embeddedness of nanoparticles can be observed in RT–35HC. Along with this, small homogeneous and heterogeneous percolation zones of GNP, GO, rGO and MWCNT mono and hybrid nanoparticles can be observed in NePCMs. The presence of similar homogeneous and heterogeneous zones of various nanoparticles used as mono and hybrid combinations have been reported in previous studies [28, 29]. The morphological features of hybrid NePCMs (NePCM$_{GO+MWCNT}$, NePCM$_{rGO+MWCNT}$ and NePCM$_{GNP+MWCNT}$) reflect the three-dimensional arrangement of hybrid combinations of GNP, GO, rGO and MWCNT nanoparticles. This three–dimensional path of hybrid nanoparticles is because of two different molecular arrangement of carbon-based additives. Since MWCNT are consisted of nested single–wall carbon nanotubes (SWCNT) of different diameters which are rolled up of multiple layers of graphite sheets to form the tubular or cylindrical shape [30]. The GO and rGO have the structure of two–dimensional layer or sheet forming the thin films

[31]. The GNP consists of short stacks of graphene sheets forming a two–dimensional nano platelet shapes which are identical to those found in the walls of carbon nanotubes, but in a planar form [32]. Therefore, this three–dimensional path of hybrid nanoparticles has a significant effect to transfer the heat in all regions of RT–35HC. In addition, two different mass ratios of GNP+MWCNT, GO+MWCNT and rGO+MWCNT hybrid nanoparticles form the different morphologies because of different molecular shapes and physical properties (i.e. density, particle size, surface area etc.) results in the good harmonious effects of heat transfer enhancement.

### *3.2. Chemical composition analysis*

Figure 5 shows the functional groups and chemical composition of GNP, GO, rGO and MWCNT nanoparticles dispersed mono and hybrid NePCMs. The structural interaction is illustrated through FTIR spectrum characterized by FTIR spectroscopy. Because of the absence of functional groups, there were no significant stretching and bending peaks observed of infrared spectra GNP, rGO and MWCNT. Despite of this, a series of absorption peaks of RT–35HC, mono and hybrid NePCMs were obtained. A series of absorption peaks were observed of pure RT–35HC and NePCMs. The spectrum of RT–35HC shows the three absorption peaks at 2955, 2913 and 2849 cm$^{-1}$ which represent the medium C–H symmetrical and anti–symmetrical stretching vibration of methyl ($-CH_3$) and methylene ($-CH_2-$) group. The peak at 1472 cm$^{-1}$ identifies the medium C–H scissoring of $-CH_2-$ and deformation of antisymmetric stretching vibration $-CH_3$ group in RT–35HC. A series of absorption peaks at 1371, 1125, and 891 cm$^{-1}$ which are due to the C–H bending and scissoring vibrations. In addition, the peak at 715 cm$^{-1}$ represents to the weak rocking vibration of C–H in long–chain methyl group. From Figure 5, it can be observed that carbon–additives mono and hybrid NePCMs reflected the consistent peaks similar that of the RT–35HC. This shows that mono and hybrid NePCMs possess the similar characteristics which RT–35HC exists without emergence of any new peak or peak shift. Therefore, the FTIR results reveal that no considerable chemical interaction occurred between the GNP, GO, rGO, MWCNT and RT–35HC. Further, there is only physical interaction between the nanoparticles and RT–35HC which illustrate that prepared mono and hybrid NePCMs are chemical stable.

### *3.3. Crystallography analysis*

The crystalline phase and dimensions of unit cell of GNP, GO, rGO, MWCNT and RT–35HC and their mono and hybrid NePCMs were analysed through crystallography analysis

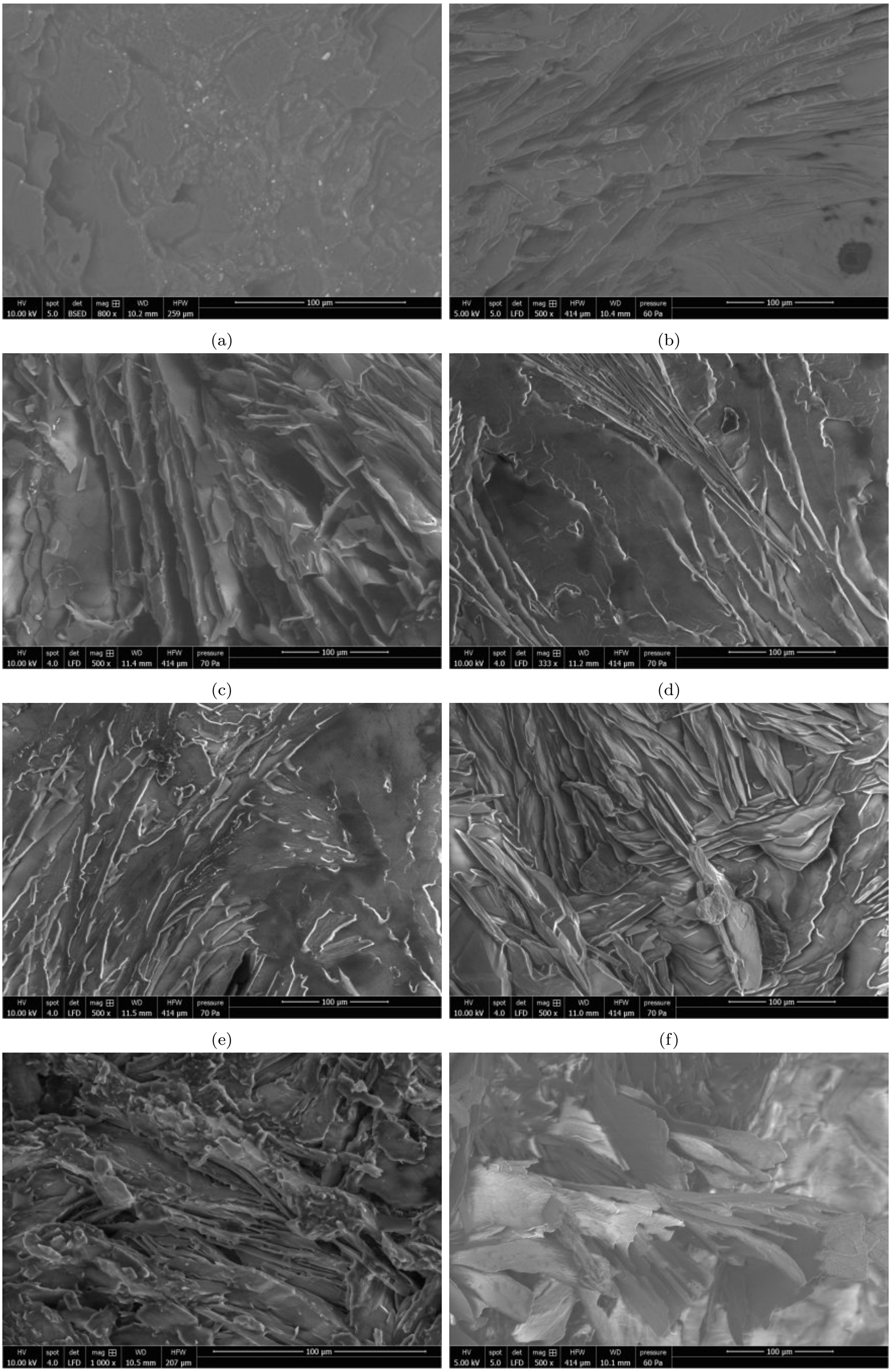

(a) (b)

(c) (d)

(e) (f)

(g) (h)

Figure 4: *ESEM images of mono and hybrid NePCMs (a) RT–35HC (b)* $NePCM_{MWCNT}$*, (c)* $NePCM_{GO}$ *(d)* $NePCM_{GO+MWCNT}$ *(e)* $NePCM_{rGO}$ *(f)* $NePCM_{rGO+MWCNT}$ *(g)* $NePCM_{GNP}$ *and (h)* $NePCM_{GNP+MWCNT}$*.*

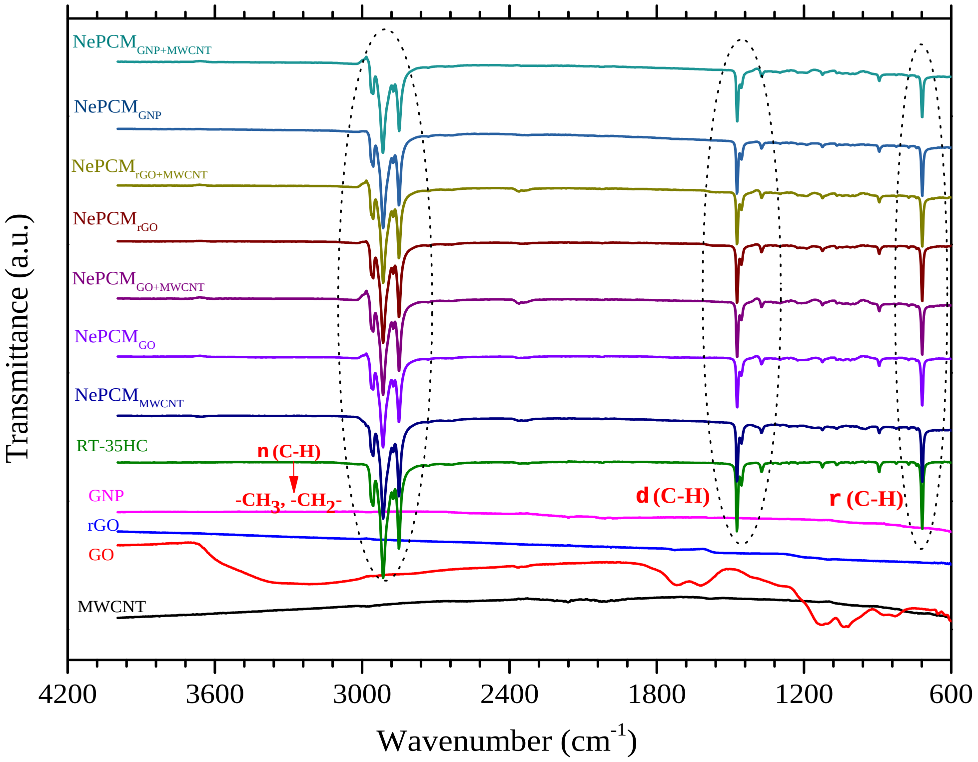

Figure 5: *FTIR spectrum of carbon–additives mono and hybrid NePCMs.*

by using XRD. Figure 6 illustrates the crystal structure XRD patterns of GNP, GO, rGO, MWCNT, RT–35HC and prepared NePCMs to confirm the presence of GNP, GO, rGO and MWCNT in RT–35HC. The XRD spectrum of MWCNTs confirmed the presence of carbon nanotubes peaks at 25.91° (002) and 42.95° (100) with the PDF No. 00-058-1638 [33]. The diffraction peak at $2\theta = 9.7°$ at reflection plane (001) confirm the presence of GO [34]. Since the rGO is the further obtained after thermochemical treatment, the diffraction peak appeared at $2\theta \approx 30°$, at reflection plane (002) [34]. The XRD pattern at 26.54°, 42.36°, 44.56° and 54.66° of corresponding reflection planes of (002), (100), (101) and (004), respectively, confirm the graphene layers of GNP with PDF No. 00-056-0159. The sharp diffraction peaks of RT-35HC was observed at 6.85° (002), 10.48° (003), 13.91° (004), 17.44° (005), 19.32° (010), 19.80° (011), 20.83° (012), 22.43° (013), 23.32° (105), 24.78° (-101), 25.65° (110), 28.12° (008), 31.75° (009), 34.75° (-110), 35.27° (0010), 39.83° (0-22), 42.73° (0012), 44.60° (207), 52.68° (220), 53.41° (-2-14) and 57.55° (-205) which attributed to the crystal planes of *n-eicosane* ($C_{20}H_{42}$) with PDF No. 00-045-1543. Although a constant and less amount of GNP,GO, rGO and MWCNT was dispersed in RT–35HC. As a consequence of this, a less significant physical changes were observed in mono and hybrid NePCMs. In addition, the XRD peaks revealed that the crystal structure of RT–35HC did not change. More further NePCM$_{MWCNT}$, NePCM$_{GO}$, NePCM$_{GO+MWCNT}$, NePCM$_{rGO}$, NePCM$_{rGO+MWCNT}$, NePCM$_{GNP}$ and NePCM$_{GNP+MWCNT}$ samples contain the peaks of GNP,GO, rGO and MWCNT.

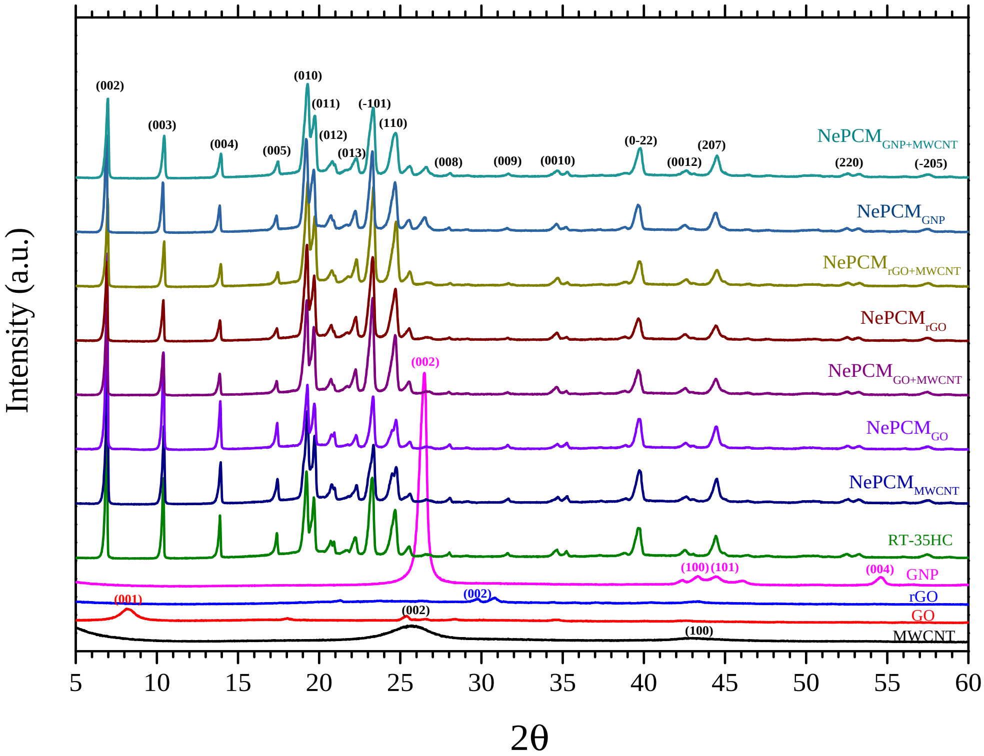

Figure 6: *XRD pattern of carbon–additives mono and hybrid NePCMs.*

### *3.4. Thermal stability analysis*

Thermal stability analysis of RT–35HC, mono and hybrid NePCMs was carried out through thermal gravimetric analysis, as shown in Figure 7. The TGA and DTGA curves of RT–35HC, mono and hybrid NePCMs are presented in Figure 7a and 7b, respectively. The thermal stability of the RT–35HC and NePCMs was estimated two parameters; (i) onset temperature degradation (T$_{onset}$) and (ii) rate of weight loss (R$_{wl}$) during kinetic process. There are four mechanisms of weight loss which include decomposition, evaporation, reduction and desorption. It can be seen from 7a and 7b that TGA and DTGA curves possess the one–step and two–step thermal degradation process, respectively. The TGA curves of RT–35HC, mono and hybrid NePCMs represent that there is no distinguishable weight loss in any sample up to ∼120°C. More further, it can be observed that by increasing temperature the rate of weight loss increases directly and reaches at the maximum degradation temperature (T$_{max.degradation}$) with constant residual ($\gamma$). In case of RT–35HC, the T$_{onset}$ and T$_{max.degradation}$ were recorded of 208.18°C and 249.29°C with 0.31% $\gamma$. During the decomposition process, the hydrocarbon chains of pure RT–35HC breakdown into monomers ($CH_3CH:CH+CH_4$) because of evaporation. The detailed summary of $T_{onset}$ and $T_{max.degradation}$ of RT–35HC, mono and hybrid NePCMs are provided in Table 2. The maximum $\gamma$ of 4.60% and 3.26% were obtained for NePCM$_{MWCNT}$ and NePCM$_{GNP+MWCNT}$, respectively, and remained constant subsequently. For mono and hybrid NePCMs, the GNP, GO, rGO, MWCNT, GNP+MWCNT, GO+MWCNT and rGO+MWCNT create a protective layer on RT–35HC surface. This protective layer delays the vaporization of RT–35HC during the thermal degradation. The DTGA curves of RT–35HC, mono and hybrid NePCMs are shown in Figure 7b and revealed that addition of GNP, GO, rGO, MWCNT, GNP+MWCNT, GO+MWCNT and rGO+MWCNT nanoparticles have improved the thermal stability. There is no decompositions was observed in samples until ∼140°C. The TGA and DTGA results revealed that hybrid NePCMs have the best thermal and chemical stability which can be potentially used for thermal management of applications. This improved capability of thermal stability can be explained by the following reasons: (i) *the* $T_{onset}$ *is related to the entire specific heat capacity of NePCMs which can be raised by the specific heat capacity of GNP, GO, rGO, MWCNT, GNP+MWCNT, GO+MWCNT and rGO+MWCNT nanoparticles*, and (ii) *enhanced thermal conductivity of NePCMs which can transfer heat faster and uniformly within the PCM* [35].

Table 2: *The decomposition temperatures and residual amount of carbon–additives mono and hybrid NePCMs.*

| Sample | $T_{onset}$ (°C) | $T_{max.degradation}$ (°C) | $\gamma$ (%) |
|---|---|---|---|
| RT-35HC | 208.18 | 249.29 | 0.31 |
| NePCM$_{MWCNT}$ | 226.15 | 262.60 | 4.60 |
| NCPCM$_{GO}$ | 225.21 | 260.60 | 0.60 |
| NePCM$_{GO+MWCNT}$ | 225.93 | 262.12 | 1.02 |
| NePCM$_{rGO}$ | 223.38 | 258.25 | 3.34 |
| NePCM$_{rGO+MWCNT}$ | 218.53 | 258.45 | 2.98 |
| NePCM$_{GNP}$ | 227.27 | 263.14 | 1.65 |
| NePCM$_{GNP+MWCNT}$ | 219.88 | 260.26 | 3.26 |

### *3.5. Phase–change thermal properties analysis*

The endothermic and exothermic peaks of RT–35HC, mono and hybrid NePCMs were analysed to determine the phase–change thermal properties, as shown in Figure 8. Figure 8a and 8b present the heating and cooling curves, respectively, of RT–35HC, mono and hybrid

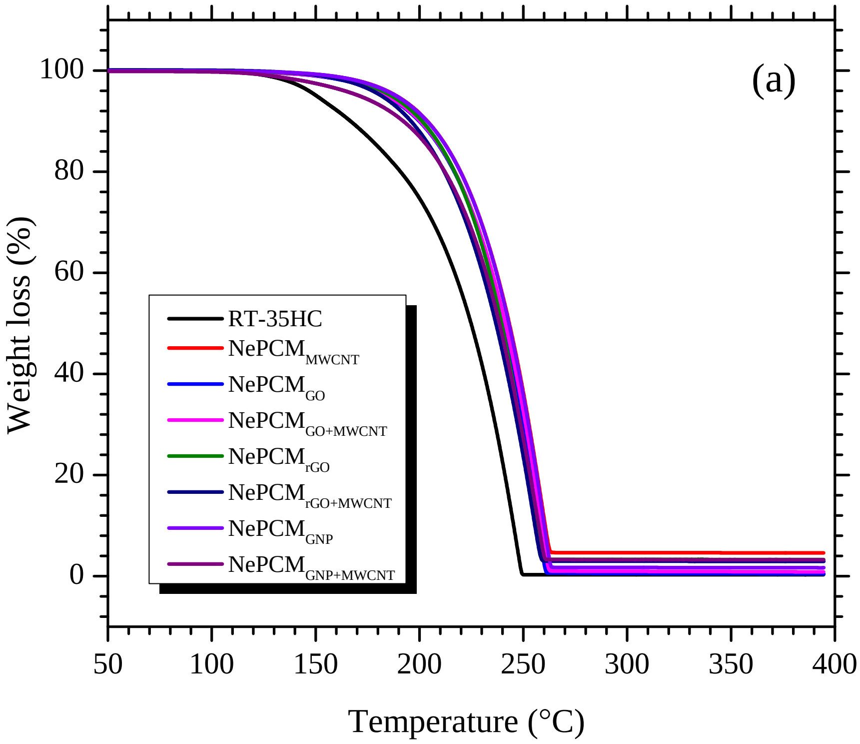

(a)

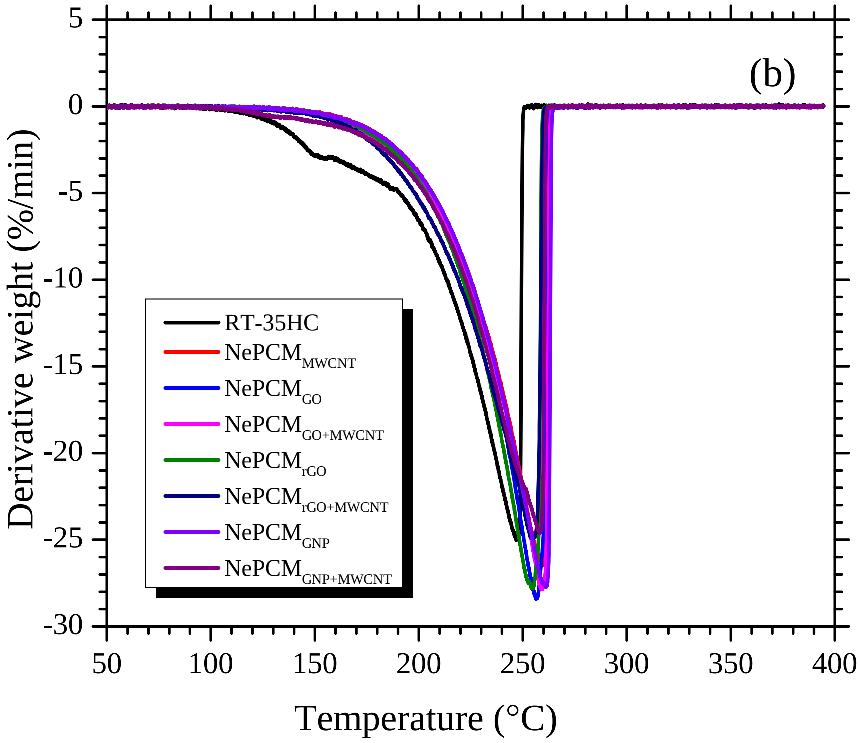

(b)

Figure 7: *(a)-TGA and (b)- DTGA thermograms of carbon–additives mono and hybrid NePCMs.*

NePCMs and measured values of latent–heat of melting/solidification and phase–transition temperatures are summarized in Table 3. There is slight variation in peak melting and solidification temperatures observed of RT–35HC because of addition of GNP, GO, rGO and MWCNT nanoparticles. Moreover, due to the addition of nanoparticles latent–heat of melting and solidification of NePCM$_{MWCNT}$, NePCM$_{GO}$, NePCM$_{GO+MWCNT}$, NePCM$_{rGO}$, NePCM$_{rGO+MWCNT}$, NePCM$_{GNP}$ and NePCM$_{GNP+MWCNT}$ were decreased expectedly. It can be revealed from Figure 8a that single endothermic peaks are obtained of RT–35HC, mono and hybrid NePCMs which is indicating an isomorphous crystalline form of RT–35HC either in a pristine state or in nanocomposite form. Contradictory, during the solidification process a bimodal crystallization behaviour is obtained of all samples. The first smaller peak represent to the crystallization temperature while second peak corresponds to the modification or transition of lattice structure from triclinc structure to the hexagonal structure [36, 37]. This two phase transformation phenomenon is attributed due to the appearance of a metastable rotator phase prior to completing the complete crystallization as a results of the heterogeneous nucleation during the cooling process [38, 29]. Below the melting temperature of paraffins always exist in crystalline form either they exist in pure single chemical compound or in composite form [39]. According to the magnitude and parity of $n$ in n–alkanes, $C_{2n}H_{2n}+2$ are crystallized in four isostructural sets for $n \geq 6$ [40]:

- Triclinic, for $n\ (even) \leq 26$ [41]
- Monoclinic, if the paraffin is pure, for $26 \leq n\ (even) \leq 36$ [42]
- Orthorhombic, if the paraffin is not pure, for $26 \leq n\ (even) \leq 36$ [42]
- Orthorhombic, for $11 \leq n\ (odd) \leq 39$ [43]

Figure 8c presents the comparison of phase–change enthalpies while melting ($\Delta H_m$) and solidification ($\Delta H_s$) of RT–35HC, mono and hybrid NePCMs. For RT–35HC, the $\Delta H_m$ and $\Delta H_s$ are obtained of 255.88 and 260.06 J/g, respectively. It can be seen that latent–heat enthalpies of hybrid NePCM were decreased higher than the mono NePCMs. The reduction in $\Delta H_m$ was obtained of 7.21%, 8.02% and 9.79% for NePCM$_{GO+MWCNT}$, NePCM$_{rGO+MWCNT}$ and NePCM$_{GNP+MWCNT}$, respectively, compared with RT–35HC. Similarly, the reduction in $\Delta H_s$ was 7.30%, 8.33% and 9.95% for NePCM$_{GO+MWCNT}$, NePCM$_{rGO+MWCNT}$ and NePCM$_{GNP+MWCNT}$, respectively, compared with RT–35HC. This reduction in $\Delta H_m$ and $\Delta H_s$ are because of the dispersion of mono (GNP, GO, rGO and MWCNT) and hybrid (GO+MWCNT, rGO+MWCNT and GNP+MWCNT) nanoparticles. The mass fraction

($\omega$) of crystallized RT–35HC in NePCMs is determined by the Equation 1:

$$\omega = \frac{\Delta H_{NePCM}}{\Delta H_{PCM}} \times 100 \tag{1}$$

Where, $\Delta H_{NePCM}$ and $\Delta H_{PCM}$ are the endothermic latent–heat of NePCM and pure PCM, respectively. While synthesising of NePCMs, mono (GNP, GO, rGO and MWCNT) and hybrid (GO+MWCNT, rGO+MWCNT and GNP+MWCNT) nanoparticles replace the RT–35HC molecules. As a consequence, the latent–heat capacity of NePCM is reduced which lead to the absorption or release of more energy.

Figure 8d presents results of degree of subcooling ($\Delta T$) of RT–35HC, mono and hybrid NePCMs. In case of RT–35HC, the peak melting ($T_m$) and crystallization ($T_c$) temperatures are obtained of 36.09 °C and 31.71 °C, respectively. The results of $\Delta T$ of mono and hyrid NePCMs revealed a fluctuating trend which is because of the type of nanoparticles. Since, the loading content of mono (GNP, GO, rGO and MWCNT) and hybrid (GO+MWCNT, rGO+MWCNT and GNP+MWCNT) nanoparticles is constant. The deviations in $T_m$ in case of hybrid for $\text{NePCM}_{GO+MWCNT}$, $\text{NePCM}_{rGO+MWCNT}$ and $\text{NePCM}_{GNP+MWCNT}$ are found of 0.06%, 1.33% and 0.22%, respectively, compared to the RT–35HC. The variation in $T_m$ and $T_c$ are due to the crystallization confinement of mono (GNP, GO, rGO and MWCNT) and hybrid (GO+MWCNT, rGO+MWCNT and GNP+MWCNT) nanoparticles surface layers within the NePCMs. In addition, the interfacial surface layers causes to form the imperfect RT–35HC and results in a slight variation in $T_m$ and $T_c$. These factors cause an increase in $\Delta T$. The heterogeneous nucleation may be favoured because of the addition of nanoparticles at the cost of crystallization point depression [38]. It has been extensively reported that the high $\Delta T$ is evidently disadvantageous for utilization of PCM in thermal management because it can result in a hysteresis response to heat transfer.

The effect of experimental and calculated latent–heats of melting and solidification of RT–35HC and NePCMs are illustrated in Figure 8e. The Equation 2 was used to calculate the theoretical values of latent–heats [44, 29]:

$$\Delta L_{NePCM} = \Delta L_{PCM} \cdot \omega = \Delta L_{PCM}(1 - \varphi) \tag{2}$$

where, $\Delta L_{NePCM}$ is the calculated latent–heat of melting and solidification of NePCM, $\Delta L_{PCM}$ represents the latent–heat of pure PCM, $\omega$ and $\varphi$ are the mass fraction of pure

PCM and nanoparticles, respectively. The results reveal that measured values of latent–heats of melting and solidification are lower than the calculated values. The deviations in values are because of the surface morphology, particle size, shape, crystal structure and thermophysical properties (i.e. density, surface area, thermal conductivity, specific heat etc.) of mono (GNP, GO, rGO and MWCNT) and hybrid (GO+MWCNT, rGO+MWCNT and GNP+MWCNT) nanoparticles. Since the mass fraction of all nanoparticles in constant in mono and hybrid NePCMs. The relative error (RE) in experimental and calculated values of latent–heat of melting and solidification was obtained of $3 \sim 9\%$ for all NePCMs, given in Table 3. Similar deviations in experimental and calculated latent–heats of melting and solidification have been reported in previous studies [29, 45, 46, 47, 44, 48, 49].

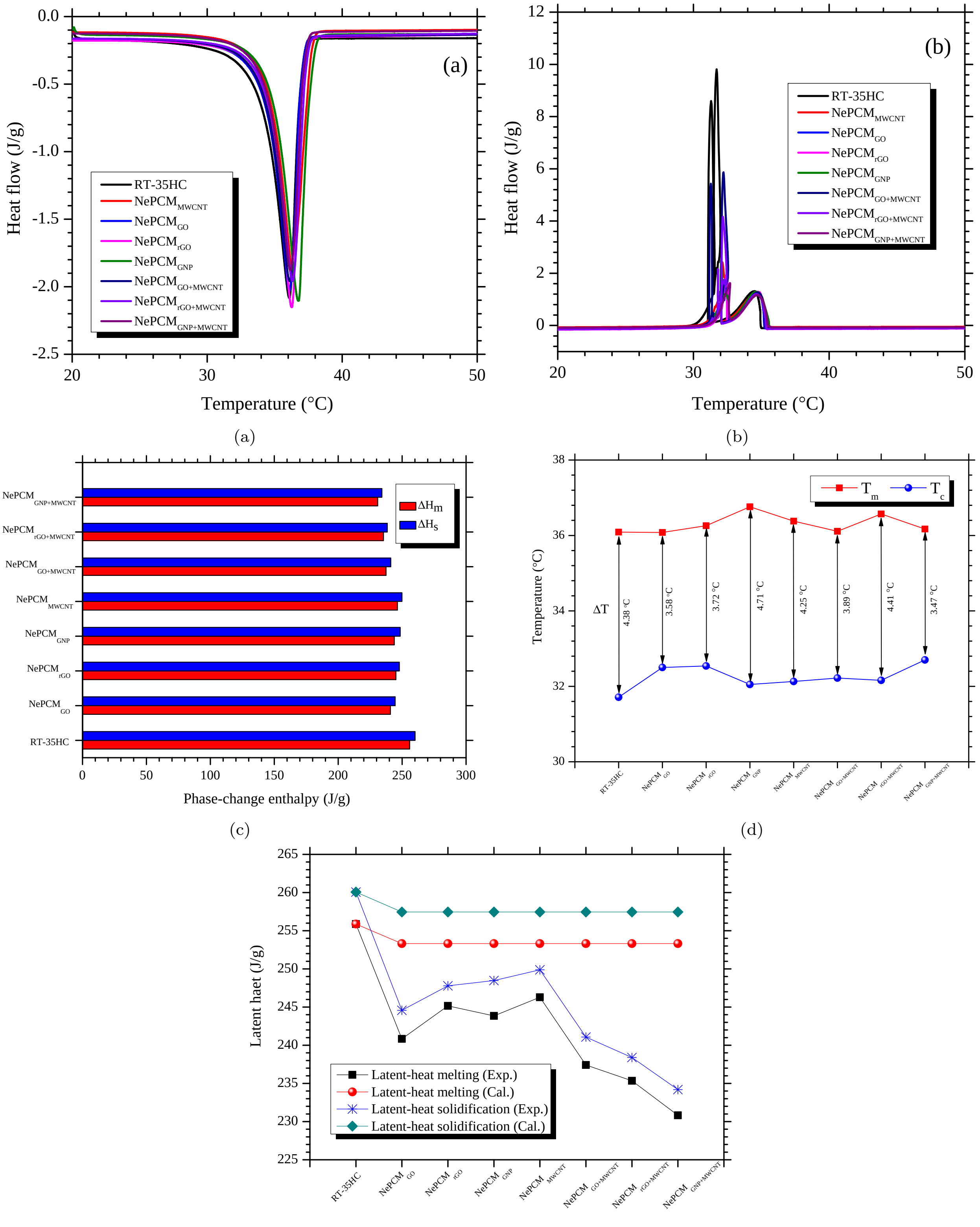

(a) (b)

(c) (d)

(e)

Figure 8: *The results of (a) heating (b) cooling (c) phase–change enthalpies (d) degree of subcooling and (e) comparison of experimental and calculated latent–heats of carbon–additives mono and hybrid NePCMs.*

Table 3: *Phase–change thermal properties of carbon–additives mono and hybrid NePCMs*.*

| Sample | Heating | | | | | Cooling | | | | | $\omega$ (%) | $\Delta$ T (°C) |
|---|---|---|---|---|---|---|---|---|---|---|---|---|
| | $T_{oset,m}$ (°C) | $T_{peak,m}$ (°C) | $\Delta H_{m,exp}$ (J/g) | $\Delta H_{m,cal}$ (J/g) | RE (%) | $T_{oset,c}$ (°C) | $T_{peak,c}$ (°C) | $\Delta H_{c,exp}$ (J/g) | $\Delta H_{c,cal}$ (J/g) | RE (%) | | |
| RT–35HC | 34.06 | 36.09 | 255.88 | - | - | 31.47 | 31.71 | 260.79 | - | - | 100.00 | 4.38 |
| $NePCM_{GO}$ | 34.31 | 36.08 | 240.83 | 253.32 | 4.93 | 32.44 | 32.50 | 244.57 | 257.46 | 5.01 | 94.12 | 3.58 |
| $NePCM_{rGO}$ | 34.47 | 36.26 | 245.16 | 253.32 | 3.22 | 32.47 | 32.54 | 247.79 | 257.46 | 3.76 | 95.81 | 3.72 |
| $NePCM_{GNP}$ | 34.81 | 36.76 | 243.85 | 253.32 | 3.74 | 31.99 | 32.05 | 248.48 | 257.46 | 3.49 | 95.30 | 4.71 |
| $NePCM_{MWCNT}$ | 34.54 | 36.38 | 246.28 | 253.32 | 2.78 | 32.03 | 32.13 | 249.88 | 257.46 | 2.94 | 96.25 | 4.25 |
| $NePCM_{GO+MWCNT}$ | 34.32 | 36.11 | 237.42 | 253.32 | 6.28 | 32.04 | 32.22 | 241.08 | 257.46 | 6.36 | 92.79 | 3.89 |
| $NePCM_{rGO+MWCNT}$ | 35.09 | 36.57 | 235.35 | 253.32 | 7.09 | 32.06 | 32.16 | 238.39 | 257.46 | 7.41 | 91.98 | 4.41 |
| $NePCM_{GNP+MWCNT}$ | 34.46 | 36.17 | 230.82 | 253.32 | 8.88 | 32.57 | 32.70 | 234.19 | 257.46 | 9.04 | 90.21 | 3.47 |

*$T_{oset,m}$: onset melting temperature, $T_{peak,m}$: peak melting temperature, $\Delta H_{m,exp}$: experimental latent-heat of melting,
$\Delta H_{m,cal}$: calculated latent-heat of melting, $T_{oset,c}$: onset solidifying temperature, $T_{peak,c}$: peak solidifying temperature,
$\Delta H_{c,exp}$: experimental latent–heat of solidifying, $\Delta H_{c,cal}$: calculated latent–heat of solidifying, RE: relative error,
$\omega$: Mass percentage of RT–35HC, $\Delta$T: Degree of subcooling

### 3.6. Thermal conductivity analysis

Thermal conductivity and thermal conductivity enhancement of RT–35HC, mono (NePCM$_{MWCNT}$, NePCM$_{GO}$, NePCM$_{rGO}$ and NePCM$_{GNP}$) and hybrid (NePCM$_{GO+MWCNT}$, NePCM$_{rGO+MWCNT}$, and NePCM$_{GNP+MWCNT}$) NePCMs were measured as a function of temperature from 20 °C to 55 °C, as shown in Figure 9. The result showed a monotonic behaviour of thermal conductivity by dispersing the MWCNT, GO, rGO and GNP nanoparticles. The thermal conductivity of NePCMs was increased because of higher thermal conductivity of MWCNT, GO, rGO and GNP nanoparticles, as shown in Figure 9a. Average thermal conductivity of RT–35HC, mono and hybrid NePCMs was measured for three different phases of solid–phase, phase–change and liquid–phase at different temperature ranges of 20–30 °C, ∼35 °C and liquid phase (40–55 °C, respectively. A constant trend was achieved in enhancement in thermal conductivity of all samples both in solid and liquid phases and higher thermal conductivity was obtained in solid phase. This shows that thermal conductivity is strongly depended on temperature change. The higher thermal conductivity in solid–phase is because of the orderly microstructure of RT–35HC, mono and hybrid NePCM compared to the disorderly microstructure exists in liquid–phase. Since, the heat flow, in solid and liquid, is associated with the lattice vibration and motion of the free electron as the molecules vibrate within their lattice structures. This lattice vibration and free electron motion is stronger in solids than the liquids. Thus, RT–35HC and NePCMs exhibit the higher thermal conductivity in solid–phase than liquid–phase. A sudden increase in thermal conductivity was observed at ∼35 °C for all samples. The phenomenon of sharp increase of thermal conductivity is associated with phase transition process of RT–35HC. At phase–transition temperature, the random motion of molecules occur within disordered microstructure of matrix in solid–liquid phase transformation. This molecular motion collapse the percolation network established by nanoparticles under the solid phase [50, 13]. In solid–phase at 20 °C, the maximum thermal conductivities of 0.214, 0.374, 0.373, 0.378, 0.354, 0.408, 0.428 and 0.443 W/m.K were obtained for RT–35HC, NePCM$_{GO}$, NePCM$_{rGO}$, NePCM$_{GNP}$, NePCM$_{MWCNT}$, NePCM$_{GO+MWCNT}$, NePCM$_{rGO+MWCNT}$, and NePCM$_{GNP+MWCNT}$, respectively. At phase–change temperature (∼35 °C), the maximum thermal conductivities were found of 0.340, 0.957, 0.935, 0.966, 0.921, 0.961, 0.965 and 0.970 W/m.K were obtained for RT–35HC, NePCM$_{GO}$, NePCM$_{rGO}$, NePCM$_{GNP}$, NePCM$_{MWCNT}$, NePCM$_{GO+MWCNT}$, NePCM$_{rGO+MWCNT}$, and NePCM$_{GNP+MWCNT}$, respectively. Since the temperature between 34–36 °C is the phase transition temperature range of RT–35HC at this point all the samples are metastable condition. At phase transformation temperature range, the crystal structure of RT–35HC becomes unstable. With the increase of temperature, the molecular vibrational motion accelerate with lattice results in increases the thermal conductivity sharply at melting temperature (∼ 35°C) [51, 13]. It be seen that hybrid NePCMs have the thermal conductivity compared to the mono NePCMs. More further, the higher thermal conductivity was achieved for NePCM$_{GNP+MWCNT}$ compared with NePCM$_{GO+MWCNT}$ and NePCM$_{rGO+MWCNT}$ in case of hybrid NePCMs. The results of percentage enhancement in thermal conductivity of mono and hybrid NePCMs is shown in Figure 7b. The Equation 3 was used to calculate the thermal conductivity enhancement factor ($\eta$) of mono and hybrid NePCMs.

$$\eta = \frac{k_{NePCM} - k_{PCM}}{k_{PCM}} \times 100 \tag{3}$$

where, $k_{NePCM}$ and $k_{PCM}$ are the thermal conductivity of the NePCM and pure PCM, respectively.

Figure 9b illustrates that the percentage enhancement of thermal conductivity increases for the case of mono and hybrid NePCMs. The Higher enhancement was achieved at phase transition temperature followed by solid–phase and then liquid–phase. The relative percentage enhancement in thermal conductivity was obtained of 74.9%, 77.7%, 77.%, 66.0%, 90.8%, 100.2%, and 107.6% for NePCM$_{GO}$, NePCM$_{rGO}$, NePCM$_{GNP}$, NePCM$_{MWCNT}$, NePCM$_{GO+MWCNT}$, NePCM$_{rGO+MWCNT}$, and NePCM$_{GNP+MWCNT}$, respectively, at 20°C compared with RT–35HC. However, the maximum enhancement in thermal conductivity was achieved at phase–change temperature of ∼ 35°C. The maximum enhancement was obtained of 181.5%, 174.9%, 184.2%, 170.7%, 182.7%, 183.8%, and 185.3% for NePCM$_{GO}$, NePCM$_{rGO}$, NePCM$_{GNP}$, NePCM$_{MWCNT}$, NePCM$_{GO+MWCNT}$, NePCM$_{rGO+MWCNT}$, and NePCM$_{GNP+MWCNT}$, respectively, compared with RT–35HC. Moreover, it can be seen from Figure 7b that hybrid NePCMs have the highest thermal conductivity enhancement compared with mono NePCMs. The variation in thermal conductivity results of mono and hybrid NePCMs is because of the surface morphology, particle size, shape, crystal structure, thermophysical properties (i.e. density, surface area, thermal conductivity, specific heat etc.) as well as the inherent thermal conductivity of mono (GNP, GO, rGO and MWCNT) and hybrid (GO+MWCNT, rGO+MWCNT and GNP+MWCNT) nanoparticles. Furthermore, the thermal boundary layer resistance between the nanoparticles and matrix molecules have significant factor of discrepancies [52].

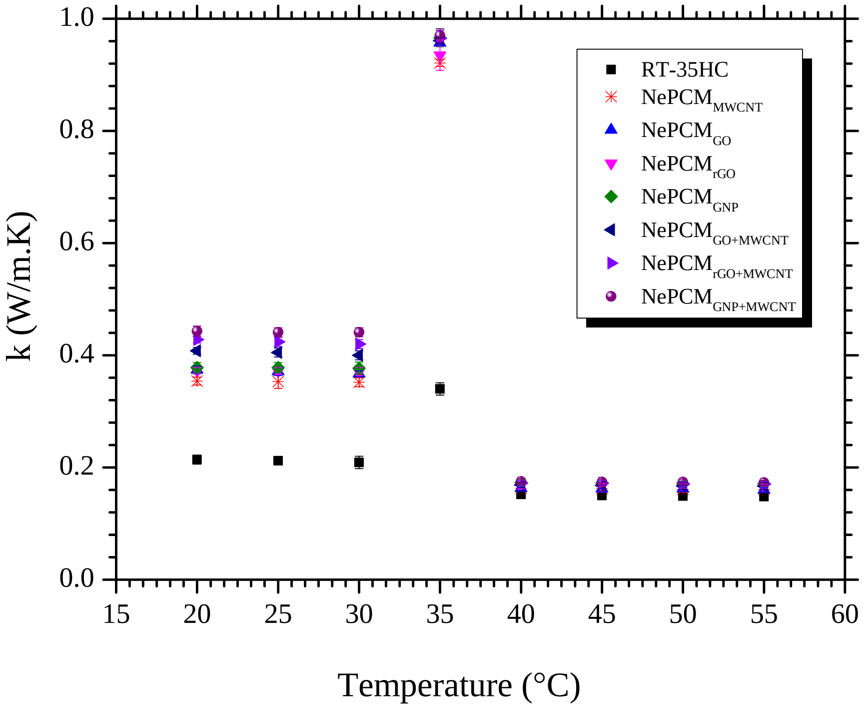

(a)

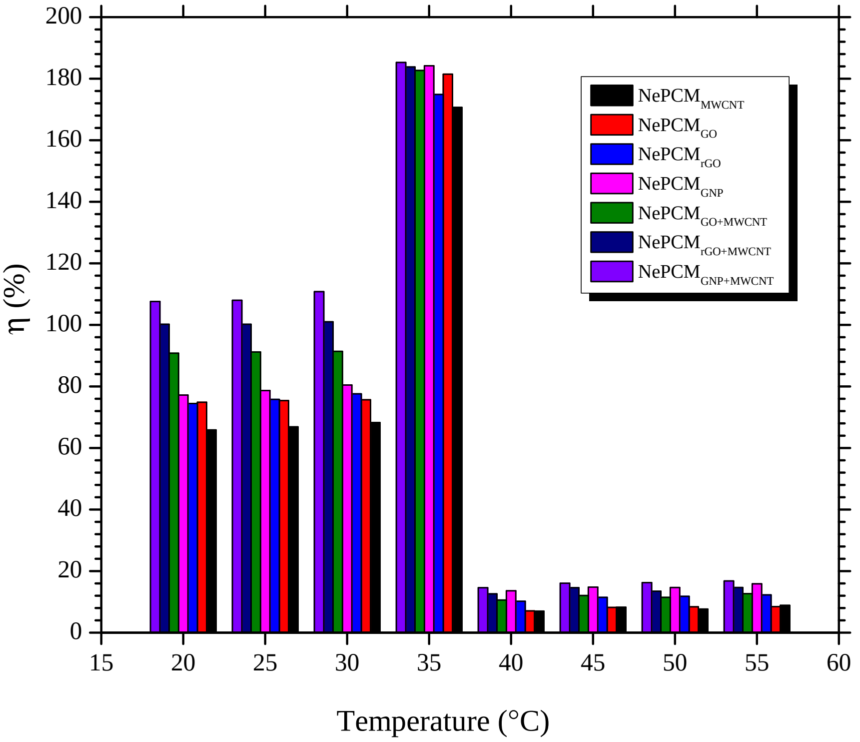

(b)

Figure 9: *The results of (a) thermal conductivity and (b) thermal conductivity enhancement factor of carbon–additives mono and hybrid NePCMs as a function of temperature.*

The thermal conductivity enhancement of NePCMs is based on several factors due to the diffusion of nanoparticles such as concentrations, Brownian motion, clustering, interfacial thermal resistance, purity, high aspect ratio and intermolecular interaction [12]. At phase transmission of NePCMs, the thermal conductivity enhancement is higher because of the constant kinetic energy despite of phase change occurrence [12]. In addition of this, the mechanism of thermal conductivity of hybrid (GO+MWCNT, rGO+MWCNT and GNP+MWCNT) nanoparticles in RT–35HC is shown Figure 10. An ideal schematic representation of 1D (MWCNT) and 2D (GO/rGO/GNP) nanoparticles structural arrangement is presented that illustrating a three–dimensional (3D) structural matrix. This 3D matrix of hybrid NePCMs form the 3D path for which the *phonon transmission* and *lattice vibration* transport the heat effectively in all directions of the RT–35HC [19, 29]. In non–metallic PCMs, the vibration of crystal lattice is the main mechanism of heat conduction. Consequently, the phonons are the main carriers of heat flow in the PCM [13]. More further, the thermal boundary resistance is reduced in hybrid NePCMs between nanoparticles and PCM which enhances the heat flow, resulting in improves of the thermal conductivity.

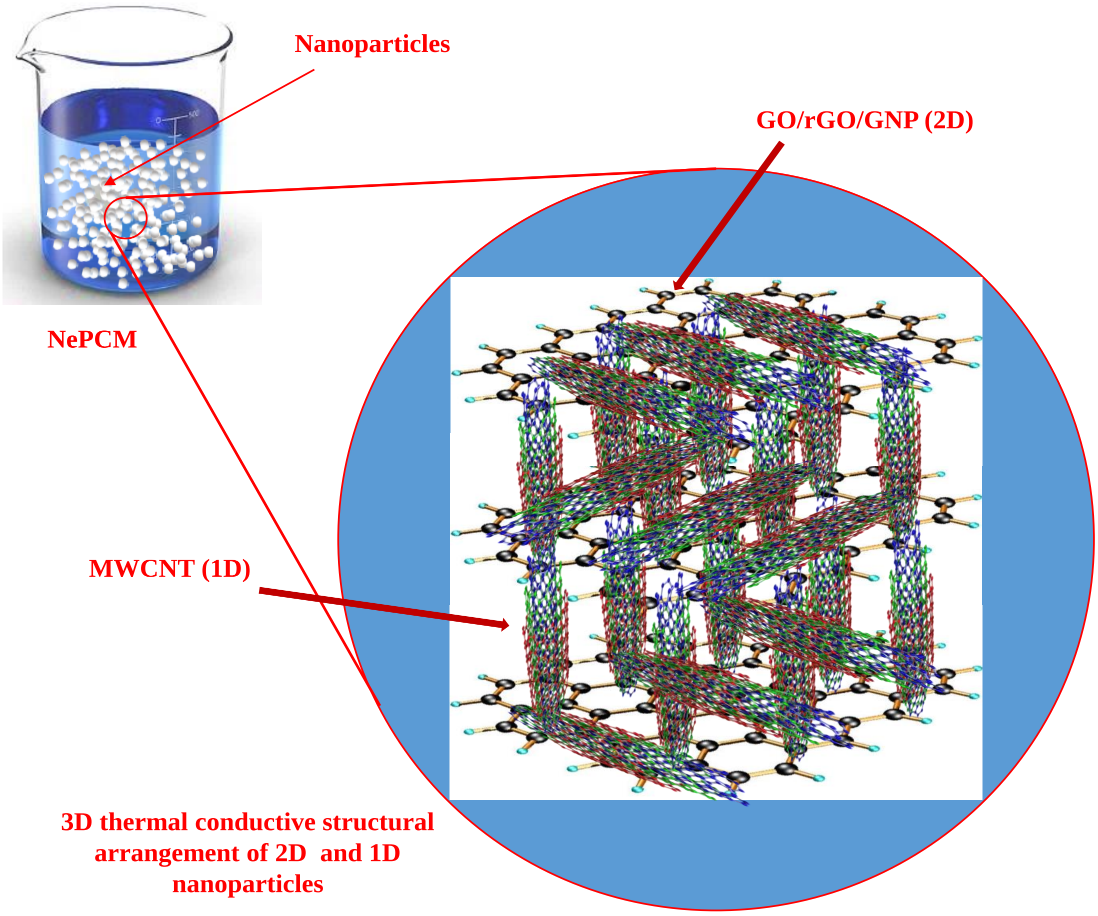

Figure 10: *Schematic representation of 3D thermal conductive arrangement of carbon–additives hybrid NePCMs.*

### 3.7. Specific heat capacity analysis

Figure 11 illustrates the specific heat capacity (C$_p$) of RT–35HC, mono and hybrid NePCMs for both solid and liquid phases. The results are presented as a function of temperature from temperature range $10-60$°C. Although the C$_p$ has less effect in total thermal energy storage density because of less thermal energy storage in sensible heating phase. However, the C$_p$ contributes the additional effects during heat transfer rate within a PCM based system, calculated by Equation 4 as follows:

$$Q = \int_{T_i}^{T_m} mC_p.dt + m\alpha_m \Delta H_m + \int_{T_m}^{T_f} mC_p.dt \tag{4}$$

where, $Q$ (J) is the quantity of total heat stored, $T_i$ (°C),$T_m$ (°C) and $T_f$ (°C) are the initial, melting and final temperatures, respectively, $m$ (kg) mass of the heat storage medium, C$_p$ (J/kg.K) is the specific heat capacity, $\alpha_m$ is the faction of melted mass and $\Delta H_m$ (J/kg) is the heat of fusion per unit mass. It can be evaluate from Equation 4 that specific heat capacity is important thermal property to investigate the heat transfer and heat storage analysis.

The comparison of C$_p$ of RT–35HC, mono and hybrid NePCMs shows that C$_p$ increases gradually with temperature between 14°C to 30°C in solid–phase while it remains constant in liquid–phase, as shown in Figure 12a and 12b, respectively. Similar trend in enhancement in C$_p$ has been reported in previous studied [28, 53, 54]. The C$_p$ of RT–35HC is obtained of 1.88 and 1.77 J/g°C for solid and liquid phases, respectively. The C$_p$ results of mono and hybrid NePCMs reveal that C$_p$ increases both in solid and liquid phases. The C$_p$ values of 2.40, 2.61, 1.77, 2.0, 2.34, 2.33 and 2.14 were determined for NePCM$_{MWCNT}$, NePCM$_{GO}$, NePCM$_{rGO}$, NePCM$_{GNP}$, NePCM$_{GO+MWCNT}$, NePCM$_{rGO+MWCNT}$, and NePCM$_{GNP+MWCNT}$, respectively, in solid–phase at 25°C. Whereas, for liquid–phase at 50°C, the C$_p$ values of 2.22, 2.25, 1.61, 2.02, 2.67, 2.65 and 2.80 were obtained for NePCM$_{MWCNT}$, NePCM$_{GO}$, NePCM$_{rGO}$, NePCM$_{GNP}$, NePCM$_{GO+MWCNT}$, NePCM$_{rGO+MWCNT}$, and NePCM$_{GNP+MWCNT}$, respectively. The polynomial equations are generated for solid phase from 14°C to 30°C for RT–35HC, mono and hybrid NePCMs after curve fitting the experimental data mentioned in Equation 5 and coefficients are given in Table 4.

$$C_P = AT^3 + BT^2 + CT + D \tag{5}$$

The comparison result of C$_p$ and C$_p$ enhancement factor ($\zeta$) of RT–35HC, mono and hy-

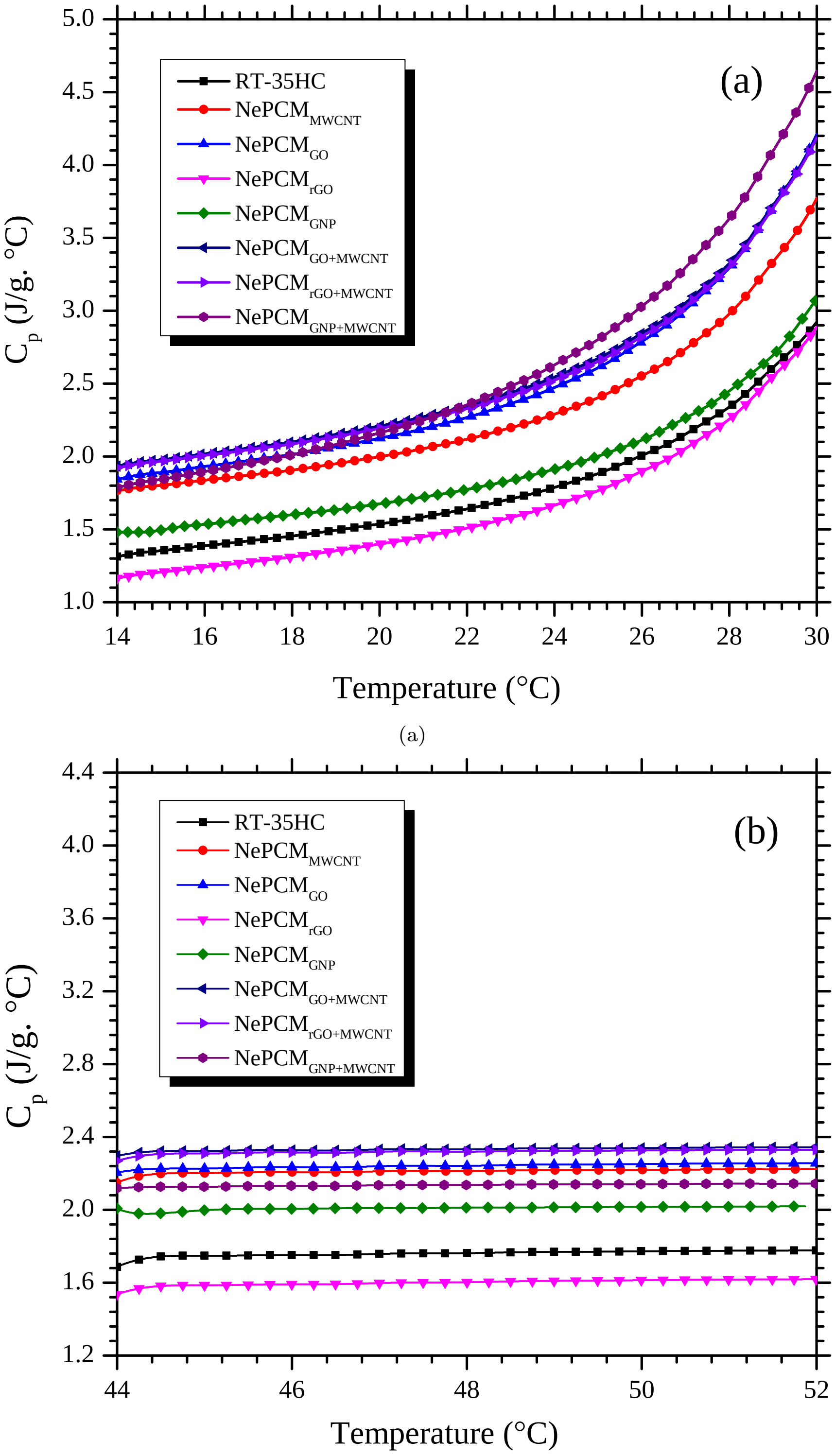

(a)

(b)

Figure 11: *Specific heat capacity curves of carbon–additives mono and hybrid NePCMs: (a) solid-phase (b) liquid-phase.*

brid NePCMs are presented in Figure **??** and **??**, respectively. The specific heat capacity enhancement factor ($\zeta$) is calculated to evaluate the effect of nanoparticles in enhancement

Table 4: *Coefficients of the third–order polynomials in solid-state, $C_p$ (J/g.°C).*

| | A | B | C | D | $R^2$ |
|---|---|---|---|---|---|
| RT-35HC | 0.0006 | -0.0349 | 0.6687 | -2.9832 | 0.9988 |
| $NePCM_{MWCNT}$ | 0.0009 | -0.0489 | 0.9319 | -4.1725 | 0.9979 |
| $NePCM_{GO}$ | 0.0010 | -0.0566 | 1.0788 | -5.0226 | 0.9981 |
| $NePCM_{rGO}$ | 0.0007 | -0.0380 | 0.7278 | -3.5055 | 0.9986 |
| $NePCM_{GNP}$ | 0.0007 | -0.0385 | 0.7426 | -3.3195 | 0.9976 |
| $NePCM_{GO+MWCNT}$ | 0.0010 | -0.0534 | 1.0192 | -4.5702 | 0.9981 |
| $NePCM_{rGO+MWCNT}$ | 0.0010 | -0.0548 | 1.0453 | -4.7404 | 0.9979 |
| $NePCM_{GNP+MWCNT}$ | 0.0010 | -0.0556 | 1.0507 | -4.9125 | 0.9990 |

of heat transfer rate in the PCM, as given by Equation 6:

$$\zeta = \frac{C_{P_{NePCM}} - C_{P_{PCM}}}{C_{P_{PCM}}} \times 100 \tag{6}$$

where, $C_{P_{NePCM}}$ and $C_{P_{PCM}}$ are the $C_p$ of the NePCM and PCM, respectively. The enhancements in $C_p$ are obtained of 27.65%, 38.54%, −6.22%, 6.37%, 24.27%, 23.58% and 13.75% for $NePCM_{MWCNT}$, $NePCM_{GO}$, $NePCM_{rGO}$, $NePCM_{GNP}$, $NePCM_{GO+MWCNT}$, $NePCM_{rGO+MWCNT}$, and $NePCM_{GNP+MWCNT}$, respectively, in solid–phase at 25°C compared to the RT–35HC. Similarly, the enhancements in $C_p$ for $NePCM_{MWCNT}$, $NePCM_{GO}$, $NePCM_{rGO}$, $NePCM_{GNP}$, $NePCM_{GO+MWCNT}$, $NePCM_{rGO+MWCNT}$, and $NePCM_{GNP+MWCNT}$ are determined of 25.21%, 27.02%, −8.95%, 13.76%, 50.81%, 49.61% and 58.09%, respectively, in liquid–phase at 50°C compared to the RT–35HC. From Figure 12, it is revealed that variations in $C_p$ are significantly depends on the type of nanoparticles and its inherent $C_p$ in pure form. In addition, the nanoparticles size, density, surface area and morphology contribute the most prominent effects in enhancement in $C_p$.

The enhancement in $C_p$ is associated with the following reasons: (i) an enhanced anharmonicity of the atomic interaction due to their volume expansion, (ii) impurities [55], (iii) the grain boundaries of nanosized materials which possess an excess volume with respect to the perfect crystal lattice and (iv) the high specific surface energies related to the high surface area of the nanoparticles per unit volume [56, 57]. Theoretically, the $C_p$ of materials is directly related to crystal structure, or its vibrational and configurational entropy which significantly affected by the nearest–neighbour configurations. Nanosized materials are structurally characterized by the metastable grain boundaries in which the nearest–neighbour configurations are much different from the coarse–grained state [56].

The anomalous enhancement in $C_p$ can be elaborated by three independent inter–molecular

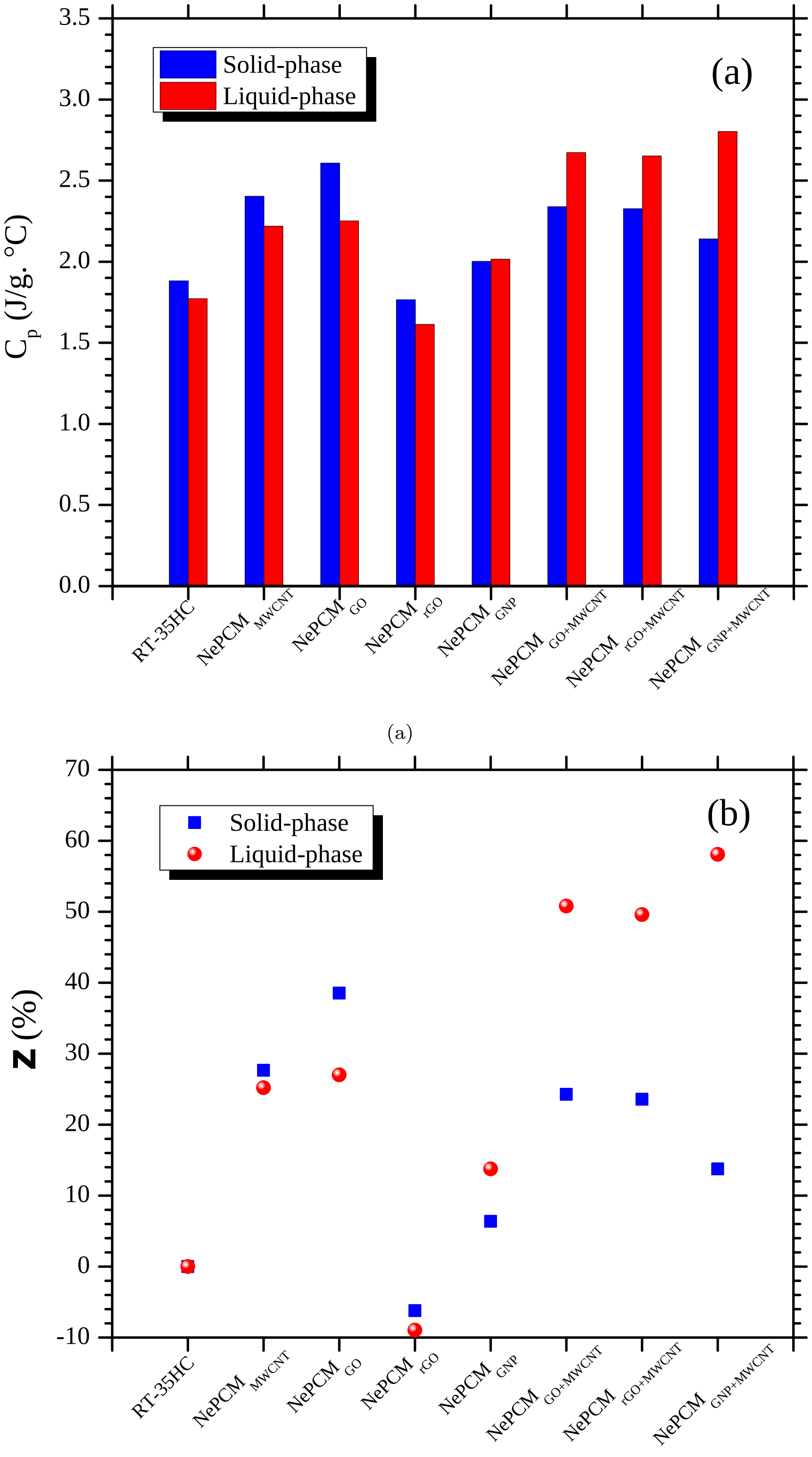

(a)

(b)

Figure 12: *(a) Comparison of specific heat capacity and (b) specific heat capacity enhancement of carbon–additives mono and hybrid NePCMs.*

403 interaction mechanisms (or modes), as shown in Figure 13

- 404 ***Higher $C_p$ of nanoparticles compared to the bulk material due to higher***

***specific surface energy*:** Since, the size of nanoparticles lies in nanometer scale and $C_p$ predicted from theoretical thermal equilibrium model for mixture, given in Equation 7, should be the function of the nominal nanoparticle diameter. In a crystalline lattice of the nanoparticles, the surface atoms are less constrained because of the less number of bonds. As the bonding between the atoms can be visualized acting like spring, the surface atoms vibrate at a higher amplitudes and lower natural frequency resulting in the higher surface energy. Therefore, phonon spectrum of nanoparticles can be analysed and have discrete numbers which depends on the size of the nanoparticles. When the size of the nanoparticles is decreased the specific heat capacity of the nanoparticles is enhanced [56, 57].

$$C_{p,t} = \frac{\phi_p \rho_p C_{p,p} + \phi_f \rho_f C_{p,f}}{\phi_p \rho_p + \phi_f \rho_f} \tag{7}$$

where, $C_{p,t}$ is the effective $C_p$ of NePCM, $C_{p,p}$ and $C_{p,f}$ are specific heat capacities nanoparticle and fluid (PCM), respectively, $\rho_p$ and $\rho_f$ are densities of nanoparticle and fluid (PCM), respectively and $\phi_p$ and $\phi_f$ are volume fractions of nanoparticle and fluid (PCM), respectively.

- ***Interfacial interaction energy of solid–fluid*:** Since, the nanoparticles have the highly surface area per unit mass which cause to increase the interfacial interaction between the nanoparticles and surrounding liquid molecules resulting in increases the interfacial thermal resistance and capacitance. This highly interfacial thermal resistance and capacitance enhance the additional thermal energy storage mechanism due to the vibrational energies between the nanoparticles atoms and adhering liquid molecules [50, 58].

- ***Adhesive semi–solid layering of liquid molecules adhering to the nanoparticles*:** The liquid molecules of molten PCM adhering on the surface of the nanoparticles create a semi–solid liquid layer. The thickness of that adhesive semi–solid liquid layers depend on the surface energy of the nanoparticles and possess smaller inter-molecular spacing on the surface compared to the higher inter-molecular spacing in the bulk liquid. Hence, this layering have higher thermal transport than the bulk PCM and increases the effective $C_p$ of NePCMs. In addition to this, the number of adhered layers of the liquid molecules are the function of surface energy of the crystalline interface. The nanoparticles of smaller size with constant weight concentration, the mass fraction of adhered semi–solid liquid layer molecules is increased proportionally on the nanoparticles surface [59, 60].

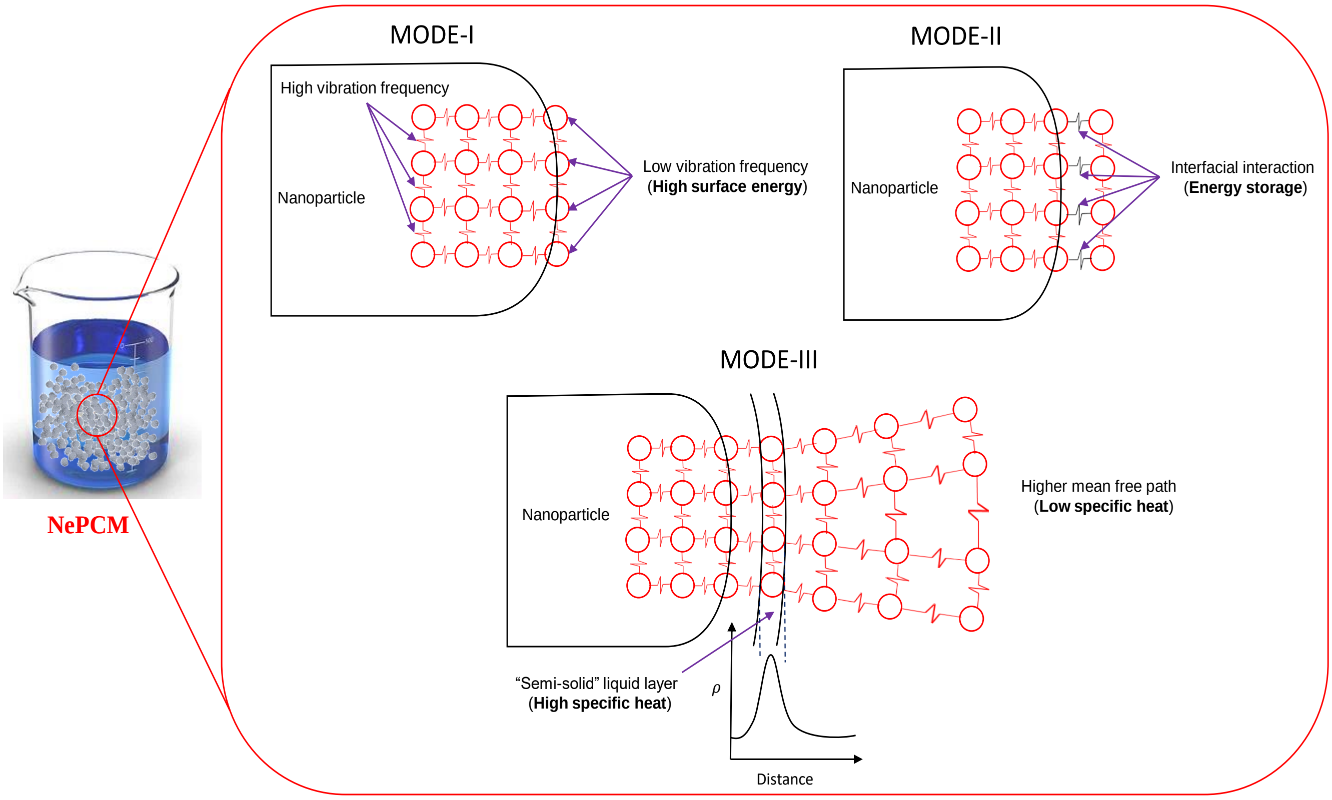

Figure 13: *Schematic representation of inter-molecular interaction modes in NePCMs causes the enhancement in specific heat capacity (a) MODE-I: High surface energy of the surface atoms in the lattice, (b) MODE-II: Interfacial interactions between the lattice atoms and liquid molecules, (c) MODE-III: A layer of semi–solid molecules adhering to the surface of lattice–atoms.*

## 4. Concluding remarks

This experimental study presents the development of carbon–additives nano–enhanced phase change materials (NePCM) for the application of efficient thermal management systems (electronics, PV modules, Li–ion batteries etc.) and solar–thermal energy storage. The two major schemes of mono (MWCNT, GO, rGO and GNP) and hybrid (GO+MWCNT, rGO+MWCNT and GNP+MWCNT) nanoparticles were dispersed in PCM (RT–35HC) having constant mass concentration of 1.0 wt.%. The chemical, physical and thermal properties were determined using ESEM, FTIR, XRD, TGA, DSC and TCA and critical findings are summarized as follows:

- The ESEM and XRD results of microstructure and crystalline phase reveal the presence of MWCNTs, GO, rGO and GNP nanoparticles in both mono and hybrid NePCMs. More further, the uniform dispersion of both mono (MWCNT, GO, rGO and GNP) and hybrid (GO+MWCNT, rGO+MWCNT and GNP+MWCNT) nanoparticles was observed in all NePCMs.

- No chemical interaction and peak shifting were observed neither in mono (NePCM$_{MWCNT}$, NePCM$_{GO}$, NePCM$_{rGO}$ and NePCM$_{GNP}$) nor in hybrid (NePCM$_{GO+MWCNT}$, NePCM$_{rGO+MWCNT}$ and NePCM$_{GNP+MWCNT}$) NePCMs. Thus, it can be proved that there is only physical interaction of all mono and hybrid nanoparticles with RT–35HC.

- The best chemical and thermal stability were achieved through TGA and DTGA analysis of all mono and hybrid NePCMs. Further, it was observed that hybrid NePCMs were more stable than mono NePCMs because of $3D$ morphological nature of hybrid (GO+MWCNT, rGO+MWCNT and GNP+MWCNT) nanoparticles.

- The enhanced thermal conductivity results were obtained of hybrid NePCM with thermal conductivities of 0.408, 0.428 and 0.443 W/m.K for NePCM$_{GO+MWCNT}$, NePCM$_{rGO+MWCNT}$, and NePCM$_{GNP+MWCNT}$, respectively, compared with mono NePCMs. The enhancement was achieved of 90.8%, 100.2% and 107.6% for for NePCM$_{GO+MWCNT}$, NePCM$_{rGO+MWCNT}$, and NePCM$_{GNP+MWCNT}$, respectively, compared to the RT–35HC. It can concluded that hybrid NePCM$_{GNP+MWCNT}$ with mass percentage ratio of 75%/25% has the highest thermal conductivity enhancement because of the optimum mass ratios, type and morphology of GNP+MWCNT nanoparticles.

- The DSC results reveal that latent–heat of fusion and solidification were decreased with the addition of both mono (MWCNT, GO, rGO and GNP) and hybrid (GO+MWCNT, rGO+MWCNT and GNP+MWCNT) nanoparticles in all NePCMs. The latent–heat of fusion for NePCM$_{GO}$, NePCM$_{rGO}$, NePCM$_{GNP}$, NePCM$_{MWCNT}$, NePCM$_{GO+MWCNT}$, NePCM$_{rGO+MWCNT}$, and NePCM$_{GNP+MWCNT}$ were obtained of 240.83, 245.16, 243.85, 246.28, 237.42, 235.35 and 230.82 J/g, respectively. The latent–heat of solidification of 244.57, 247.79, 248.48, 249.88, 241.08, 238.39 and 234.19 J/g were predicted for NePCM$_{GO}$, NePCM$_{rGO}$, NePCM$_{GNP}$, NePCM$_{MWCNT}$, NePCM$_{GO+MWCNT}$, NePCM$_{rGO+MWCNT}$, and NePCM$_{GNP+MWCNT}$, respectively. Since, the hybrid NePCM$_{GNP+MWCNT}$ has the thermal conductivity and optimum capacity of latent–heat of fusion/solidification, the less degree of subcooling of 3.47°C was achieved which showed the best NePCM melting and cooling heat transfer process. The deviation in peak melting temperature was observed of 0.22% for hybrid NePCM$_{GNP+MWCNT}$.

- The specific heat capacity results of mono and hybrid NePCMs reveal the increasing trends of compared with RT–35HC. The enhancement of 13.75% was achieved with hybrid NePCM$_{GNP+MWCNT}$ compared to RT–35HC in solid–phase. The enhancement in specific heat capacity is based on three modes: (i) higher specific heat of nanoparticles, (ii) interfacial interactional layers between solid-liquid and (iii) semi–solid liquid layers of molecules adhering to the surface of nanoparticles.

From the above mention key findings conclude and suggest that carbon–additives hybrid nanoparticles (GO+MWCNT, rGO+MWCNT and GNP+MWCNT) dispersed NePCMs have the best thermal performance in terms of thermal management and thermal energy storage. More specially, the GNP+MWCNT dispersed hybrid NePCM has the optimum capacity of latent–heat storage and higher thermal conductivity which improve the heat transfer rate in conduction and convection modes and heat absorption capacity. Hence, hybrid NePCMs can be potentially used for thermal management and thermal storage applications.

## Conflict of interest

The authors declare no conflict of interest regarding this research article.

## 5. Acknowledgement

This research is facilitated by the Faculty of Engineering, University of Nottingham, UK research infrastructure. The corresponding author (Adeel Arshad) acknowledges University of Nottingham for awarding him the *Faculty of Engineering Research Excellence PhD Scholarship* to pursue a Ph.D. research program. The authors acknowledge the use of facilities at Nanoscale and Microscale Research Centre of the University of Nottingham supported by Engineering and Physical Sciences Research Council [grant number EP/L022494/1]. The authors wish to thank 2–Dtech Ltd/Versarien PLC, UK for providing graphene nanoplatelets (GNPs), graphene oxide (GO) and reduced graphene oxide (rGO) used in this study. The project is also supported by H2020-MSCA-RISE-778104-ThermaSMART.

## References

[1] H. M. Ali, A. Arshad, M. M. Janjua, W. Baig, U. Sajjad, Thermal performance of LHSU for electronics under steady and transient operations modes, International Journal of Heat and Mass Transfer 127 (2018) 1223–1232. `doi:10.1016/j.ijheatmasstransfer.2018.06.120`.

[2] A. Arshad, M. Jabbal, Y. Yan, J. Darkwa, The micro-/nano-pcms for thermal energy storage systems: A state of art review, International Journal of Energy Research 43 (11) (2019) 5572–5620. `arXiv:https://onlinelibrary.wiley.com/doi/pdf/10.1002/er.4550`, `doi:10.1002/er.4550`.
URL `https://onlinelibrary.wiley.com/doi/abs/10.1002/er.4550`

[3] C. Xiao, G. Zhang, Z. Li, X. Yang, Custom design of solid–solid phase change material with ultra-high thermal stability for battery thermal management, Journal of Materials Chemistry A 8 (29) (2020) 14624–14633. `doi:10.1039/d0ta05247g`.

[4] Y. Lv, G. Liu, G. Zhang, X. Yang, A novel thermal management structure using serpentine phase change material coupled with forced air convection for cylindrical battery modules, Journal of Power Sources 468 (2020) 228398. `doi:10.1016/j.jpowsour.2020.228398`.

[5] J. He, X. Yang, G. Zhang, A phase change material with enhanced thermal conductivity and secondary heat dissipation capability by introducing a binary thermal conductive skeleton for battery thermal management, Applied Thermal Engineering 148 (2019) 984–991. `doi:10.1016/j.applthermaleng.2018.11.100`.

[6] Y. Lv, X. Yang, G. Zhang, Durability of phase-change-material module and its relieving effect on battery deterioration during long-term cycles, Applied Thermal Engineering 179 (2020) 115747. `doi:10.1016/j.applthermaleng.2020.115747`.

[7] A. Arshad, M. Jabbal, Y. Yan, Thermal performance of PCM-based heat sink with partially filled copper oxide coated metal-foam for thermal management of microelectronics, in: 2020 19th IEEE Intersociety Conference on Thermal and Thermomechanical Phenomena in Electronic Systems (ITherm), IEEE, 2020. `doi:10.1109/itherm45881.2020.9190574`.

[8] H. M. Ali, A. Arshad, Experimental investigation of n-eicosane based circular pin-fin heat sinks for passive cooling of electronic devices, International Journal of Heat and Mass Transfer 112 (2017) 649–661. `doi:10.1016/j.ijheatmasstransfer.2017.05.004`.

[9] N. Putra, A. F. Sandi, B. Ariantara, N. Abdullah, T. M. I. Mahlia, Performance of beeswax phase change material (PCM) and heat pipe as passive battery cooling system for electric vehicles, Case Studies in Thermal Engineering 21 (2020) 100655. `doi:10.1016/j.csite.2020.100655`.

[10] C. Zhang, M. Yu, Y. Fan, X. Zhang, Y. Zhao, L. Qiu, Numerical study on heat transfer enhancement of PCM using three combined methods based on heat pipe, Energy 195 (2020) 116809. `doi:10.1016/j.energy.2019.116809`.

[11] C. Buzea, I. Pacheco, Nanomaterials and their classification, in: Advanced Structured Materials, Springer India, 2016, pp. 3–45. `doi:10.1007/978-81-322-3655-9_1`.

[12] B. E. Jebasingh, A. V. Arasu, A comprehensive review on latent heat and thermal conductivity of nanoparticle dispersed phase change material for low-temperature applications, Energy Storage Materials 24 (2020) 52–74. `doi:10.1016/j.ensm.2019.07.031`.

[13] S. Wu, T. Yan, Z. Kuai, W. Pan, Thermal conductivity enhancement on phase change materials for thermal energy storage: A review, Energy Storage Materials 25 (2020) 251–295. `doi:10.1016/j.ensm.2019.10.010`.

[14] D. H. Choi, J. Lee, H. Hong, Y. T. Kang, Thermal conductivity and heat transfer performance enhancement of phase change materials (PCM) containing carbon additives for heat storage application, International Journal of Refrigeration 42 (2014) 112–120. `doi:10.1016/j.ijrefrig.2014.02.004`.

[15] M. Li, M. Chen, Z. Wu, J. Liu, Carbon nanotube grafted with polyalcohol and its influence on the thermal conductivity of phase change material, Energy Conversion and Management 83 (2014) 325–329. `doi:10.1016/j.enconman.2014.04.002`.

[16] T. Li, J.-H. Lee, R. Wang, Y. T. Kang, Heat transfer characteristics of phase change nanocomposite materials for thermal energy storage application, International Journal of Heat and Mass Transfer 75 (2014) 1–11. `doi:10.1016/j.ijheatmasstransfer.2014.03.054`.

[17] L.-W. Fan, Z.-Q. Zhu, Y. Zeng, Y.-Q. Xiao, X.-L. Liu, Y.-Y. Wu, Q. Ding, Z.-T. Yu, K.-F. Cen, Transient performance of a PCM-based heat sink with high aspect-ratio carbon nanofillers, Applied Thermal Engineering 75 (2015) 532–540. `doi:10.1016/j.applthermaleng.2014.10.050`.

[18] F. Bahiraei, A. Fartaj, G.-A. Nazri, Experimental and numerical investigation on the performance of carbon-based nanoenhanced phase change materials for thermal management applications, Energy Conversion and Management 153 (2017) 115–128. `doi:10.1016/j.enconman.2017.09.065`.

[19] D. Zou, X. Ma, X. Liu, P. Zheng, Y. Hu, Thermal performance enhancement of composite phase change materials (PCM) using graphene and carbon nanotubes as additives for the potential application in lithium-ion power battery, International Journal of Heat and Mass Transfer 120 (2018) 33–41. `doi:10.1016/j.ijheatmasstransfer.2017.12.024`.

[20] C. Li, B. Zhang, B. Xie, X. Zhao, J. Chen, Tailored phase change behavior of na2so4·10h2o/expanded graphite composite for thermal energy storage, Energy Conversion and Management 208 (2020) 112586. `doi:10.1016/j.enconman.2020.112586`.

[21] 2-dtech ltd/versarien plc, uk., accessed: 01/04/2020.
URL `https://www.2-dtech.com/products/`

[22] Industrial multi-walled carbon nanotubes (gcm597), carbon nanotubes plus, accessed: 01/04/2020.
URL `https://cnplus.us/inc/sdetail/403`

[23] Pcm rt-line, rt35hc, rubitherm technologies gmbh, accessed: 16/11/2020.
URL `https://www.rubitherm.eu/en/index.php/productcategory/organische-pcm-rt`

[24] A. Arshad, M. Jabbal, Y. Yan, D. Reay, A review on graphene based nanofluids: Preparation, characterization and applications, Journal of Molecular Liquids 279 (2019) 444–484. `doi:10.1016/j.molliq.2019.01.153`.

[25] Tci thermal conductivity analyzer, c-therm technologies ltd. canada, accessed: 01/05/2020.
URL `https://ctherm.com/products/tci_thermal_conductivity/`

[26] Ta instruments sdt-q600 simultaneous tga / dsc, artisan technology group, usa, accessed: 01/05/2020.
URL `https://www.artisantg.com/Scientific/74393-1/TA_Instruments_SDT_Q600_Simultaneous_TGA_DSC`

[27] Dsc 2500, ta instruments, uk, accessed: 01/05/2020.
URL `https://www.tainstruments.com/dsc-2500/`

[28] M. Chieruzzi, A. Miliozzi, T. Crescenzi, L. Torre, J. M. Kenny, A new phase change material based on potassium nitrate with silica and alumina nanoparticles for thermal energy storage, Nanoscale research letters 10 (1) (2015) 273.

[29] A. Arshad, M. Jabbal, Y. Yan, Preparation and characteristics evaluation of mono and hybrid nano-enhanced phase change materials (NePCMs) for thermal management of microelectronics, Energy Conversion and Management 205 (2020) 112444. `doi:10.1016/j.enconman.2019.112444`.

[30] A. Aqel, K. M. A. El-Nour, R. A. Ammar, A. Al-Warthan, Carbon nanotubes, science and technology part (i) structure, synthesis and characterisation, Arabian Journal of Chemistry 5 (1) (2012) 1–23. `doi:10.1016/j.arabjc.2010.08.022`.

[31] G. Wypych, PRODUCTION OF GRAPHENE AND ITS DERIVATIVES, in: Graphene, Elsevier, 2019, pp. 9–84. `doi:10.1016/b978-1-927885-51-2.50005-5`.

[32] P. Cataldi, A. Athanassiou, I. Bayer, Graphene nanoplatelets-based advanced materials and recent progress in sustainable applications, Applied Sciences 8 (9) (2018) 1438. `doi:10.3390/app8091438`.

[33] T. M. Keller, S. B. Qadri, C. A. Little, Carbon nanotube formation in situ during carbonization in shaped bulk solid cobalt nanoparticle compositions, Journal of Materials Chemistry 14 (20) (2004) 3063. `doi:10.1039/b402936d`.

[34] G. Yasin, M. Arif, M. Shakeel, Y. Dun, Y. Zuo, W. Q. Khan, Y. Tang, A. Khan, M. Nadeem, Exploring the nickel-graphene nanocomposite coatings for superior corrosion resistance: Manipulating the effect of deposition current density on its morphology, mechanical properties, and erosion-corrosion performance, Advanced Engineering Materials 20 (7) (2018) 1701166. `doi:10.1002/adem.201701166`.

[35] Y. Chen, W. Luo, J. Wang, J. Huang, Enhanced thermal conductivity and durability of a paraffin wax nanocomposite based on carbon-coated aluminum nanoparticles, The Journal of Physical Chemistry C 121 (23) (2017) 12603–12609. `doi:10.1021/acs.jpcc.7b02651`.

[36] S. Kolesnikov, Z. Syunyaev, Phase transitions in the melting and crystallization of n-c//1//8h//3//8 and n-c//2//0h//4//2., Journal of applied chemistry of the USSR 58 (10 pt 2) (1985) 2097–2101, cited By 6.
URL `https://www.scopus.com/inward/record.uri?eid=2-s2.0-0022139277&partnerID=40&md5=551e7d7b9ca91cd165c094dd5f823991`

[37] R. M. A. Ghossein, M. S. Hossain, J. Khodadadi, Experimental determination of temperature-dependent thermal conductivity of solid eicosane-based silver nanostructure-enhanced phase change materials for thermal energy storage, International Journal of Heat and Mass Transfer 107 (2017) 697–711. `doi:10.1016/j.ijheatmasstransfer.2016.11.059`.

[38] F. Yavari, H. R. Fard, K. Pashayi, M. A. Rafiee, A. Zamiri, Z. Yu, R. Ozisik, T. Borca-Tasciuc, N. Koratkar, Enhanced thermal conductivity in a nanostructured phase change composite due to low concentration graphene additives, The Journal of Physical Chemistry C 115 (17) (2011) 8753–8758. `doi:10.1021/jp200838s`.

[39] M. Nabil, J. Khodadadi, Experimental determination of temperature-dependent thermal conductivity of solid eicosane-based nanostructure-enhanced phase change materials, International Journal of Heat and Mass Transfer 67 (2013) 301–310. `doi:10.1016/j.ijheatmasstransfer.2013.08.010`.

[40] S. C. Nyburg, J. A. Potworowski, Prediction of unit cells and atomic coordinates for the n-alkanes, Acta Crystallographica Section B Structural Crystallography and Crystal Chemistry 29 (2) (1973) 347–352. `doi:10.1107/s0567740873002451`.

[41] A. Mller, K. Lonsdale, The low-temperature form of c18h38, Acta Crystallographica 1 (3) (1948) 129–131. `doi:10.1107/s0365110x4800034x`.

[42] M. G. Broadhurst, An analysis of the solid phase behavior of the normal paraffins, J. Res. Natl. Bur. Stand., Sect. A 66 (3) (1962) 241–249.

[43] S. H. PIPER, T. MALKIN, Crystal structure of normal paraffins, Nature 126 (3173) (1930) 278–278. `doi:10.1038/126278b0`.

[44] H. Tian, W. Wang, J. Ding, X. Wei, M. Song, J. Yang, Thermal conductivities and characteristics of ternary eutectic chloride/expanded graphite thermal energy storage composites, Applied Energy 148 (2015) 87–92. `doi:10.1016/j.apenergy.2015.03.020`.

[45] A. Sarı, A. Karaipekli, C. Alkan, Preparation, characterization and thermal properties of lauric acid/expanded perlite as novel form-stable composite phase change material, Chemical Engineering Journal 155 (3) (2009) 899–904. `doi:10.1016/j.cej.2009.09.005`.

[46] J. Wang, H. Xie, Z. Xin, Thermal properties of paraffin based composites containing multi-walled carbon nanotubes, Thermochimica Acta 488 (1-2) (2009) 39–42. `doi:10.1016/j.tca.2009.01.022`.

[47] S. Wu, D. Zhu, X. Zhang, J. Huang, Preparation and melting/freezing characteristics of cu/paraffin nanofluid as phase-change material (PCM), Energy & Fuels 24 (3) (2010) 1894–1898. `doi:10.1021/ef9013967`.

[48] R. Sharma, P. Ganesan, V. Tyagi, H. Metselaar, S. Sandaran, Thermal properties and heat storage analysis of palmitic acid-TiO 2 composite as nano-enhanced organic phase change material (NEOPCM), Applied Thermal Engineering 99 (2016) 1254–1262. `doi:10.1016/j.applthermaleng.2016.01.130`.

[49] X. Li, Y. Zhou, H. Nian, X. Zhang, O. Dong, X. Ren, J. Zeng, C. Hai, Y. Shen, Advanced nanocomposite phase change material based on calcium chloride hexahydrate with aluminum oxide nanoparticles for thermal energy storage, Energy & Fuels 31 (6) (2017) 6560–6567. `doi:10.1021/acs.energyfuels.7b00851`.

[50] R. Prasher, P. Bhattacharya, P. E. Phelan, Brownian-motion-based convective-conductive model for the effective thermal conductivity of nanofluids, Journal of Heat Transfer 128 (6) (2005) 588–595. `doi:10.1115/1.2188509`.

[51] J. Wang, H. Xie, Z. Xin, Y. Li, L. Chen, Enhancing thermal conductivity of palmitic acid based phase change materials with carbon nanotubes as fillers, Solar Energy 84 (2) (2010) 339–344. `doi:10.1016/j.solener.2009.12.004`.

[52] O. Mahian, L. Kolsi, M. Amani, P. Estellé, G. Ahmadi, C. Kleinstreuer, J. S. Marshall, M. Siavashi, R. A. Taylor, H. Niazmand, S. Wongwises, T. Hayat, A. Kolanjiyil, A. Kasaeian, I. Pop, Recent advances in modeling and simulation of nanofluid flows-part i: Fundamentals and theory, Physics Reports 790 (2019) 1–48. `doi:10.1016/j.physrep.2018.11.004`.

[53] M. Mehrali, S. T. Latibari, M. Mehrali, T. M. I. Mahlia, E. Sadeghinezhad, H. S. C. Metselaar, Preparation of nitrogen-doped graphene/palmitic acid shape stabilized composite phase change material with remarkable thermal properties for thermal energy storage, Applied Energy 135 (2014) 339–349. `doi:10.1016/j.apenergy.2014.08.100`.

[54] A. A. Aydın, A. Aydın, High-chain fatty acid esters of 1-hexadecanol for low temperature thermal energy storage with phase change materials, Solar Energy Materials and Solar Cells 96 (2012) 93–100. `doi:10.1016/j.solmat.2011.09.013`.

[55] E. Hellstern, H. J. Fecht, Z. Fu, W. L. Johnson, Structural and thermodynamic properties of heavily mechanically deformed ru and AlRu, Journal of Applied Physics 65 (1) (1989) 305–310. `doi:10.1063/1.342541`.

[56] L. Wang, Z. Tan, S. Meng, D. Liang, G. Li, Enhancement of molar heat capacity of nanostructured al2o3, Journal of Nanoparticle Research 3 (5/6) (2001) 483–487. `doi:10.1023/a:1012514216429`.

[57] B.-X. Wang, L.-P. Zhou, X.-F. Peng, Surface and size effects on the specific heat capacity of nanoparticles, International Journal of Thermophysics 27 (1) (2006) 139–151. `doi:10.1007/s10765-006-0022-9`.

[58] L. Xue, P. Keblinski, S. Phillpot, S.-S. Choi, J. Eastman, Effect of liquid layering at the liquid–solid interface on thermal transport, International Journal of Heat and Mass Transfer 47 (19-20) (2004) 4277–4284. `doi:10.1016/j.ijheatmasstransfer.2004.05.016`.

[59] S. H. Oh, Ordered liquid aluminum at the interface with sapphire, Science 310 (5748) (2005) 661–663. `doi:10.1126/science.1118611`.

[60] D. Shin, D. Banerjee, Enhancement of specific heat capacity of high-temperature silica-nanofluids synthesized in alkali chloride salt eutectics for solar thermal-energy storage

applications, International Journal of Heat and Mass Transfer 54 (5-6) (2011) 1064–1070. `doi:10.1016/j.ijheatmasstransfer.2010.11.017`.